Chemical Engineering Journal 496 (2024) 154314

Contents lists available at ScienceDirect

Chemical Engineering Journal

journal homepage: www.elsevier.com/locate/cej

Evolution of the Pd^0/PdO phase change on Pd-MCM-41 catalyst for efficient production of furfural from the fast pyrolysis of cellulose

Jingwei Wang [a], Qiaoqiao Zhou [b], Jinxing Gu [a], Sasha Yang [a], Qinfen Gu [c], Anthony De Girolamo [a], Lian Zhang [a,*]

[a] Department of Chemical & Biological Engineering, Monash University, Wellington Road, Clayton, Victoria, Australia
[b] State Key Laboratory of Materials-Oriented Chemical Engineering, College of Chemical Engineering, Nanjing Tech University, Nanjing 211816, Jiangsu, China
[c] Australian Synchrotron, ANSTO, 800 Blackburn Road, Clayton, Victoria, Australia

ARTICLE INFO

Keywords:
Furfural
Cellulose
Fast pyrolysis
Surface hydrophilicity
Phase change of Pd
Structural reversion

ABSTRACT

Furfural ($C_5H_4O_2$) is a high-value platform chemical that is traditionally derived from the solvolysis of hemicellulose. However, its production from pyrolysis is far from satisfactory. In particular, the abundant cellulose within lignocellulosic biomass has yet to be successfully upgraded into furfural. Consequently, the overall yield of furfural from a lignocellulosic biomass is extremely low. Herein, we report a facile heterogeneous catalyst prepared from a simple impregnation of palladium (Pd) onto MCM-41 mesoporous silica. The catalyst demonstrated a remarkably high selectivity of ~58.5% and yield of ~32.5 wt% for furfural from the fast pyrolysis of wet cellulose. It was also confirmed to reach a selectivity of 65.4% and yield of 44.5 wt% for furfural from wet xylan, as well as a furfural yield of 23.9 wt% from wet sugarcane bagasse. All these values are superior to the literature reports. Through advanced characterisation including in-situ synchrotron high-temperature XRD and DRIFTS measurement, the loading of Pd in a tiny quantity of 1 mol% was confirmed to be sufficient in enhancing the surface hydrophilicity of the MCM-41 support, promoting the adsorption of reactants especially the formaldehyde group (HCHO), as well as the desorption of the target product furfural. In addition, Pd oxide (i.e., $Pd^{2+}O$) was confirmed to be the catalytic active site. However, it was partly reduced into metallic Pd^0 during the cellulose pyrolysis, due to the preferred reduction by adsorbed formaldehyde group and other reductants including H_2 and CO in the vicinity of the PdO sites on the Pd-O-Si interface. Nevertheless, the catalyst was proven to retain the memory of its initial state after combustive regeneration in air, having oxidation state of Pd, particle size, and dispersion degree being reversed to its original construction. Accordingly, its activity remained stable upon cyclic testing. All these results demonstrate a high practical viability of this heterogenous catalyst for the valorisation of cellulose-rich biomass, an otherwise abundant crop waste across the world.

1. Introduction

Biomass is an abundant renewable source that can convert into various value-added products such as bio-oil and platform chemicals [1]. Out of the twelve platform chemicals defined by the Department of Energy, USA [2–5], furfural ($C_5H_4O_2$) has a broad range of applications in the production of critical end-use chemicals such as pharmaceuticals, resins, food, and fuel additives. Its global market reached $817.9 million in 2022 and is further forecast to grow at a compound annual rate of 4.2% up to 2028 [6]. Nevertheless, regarding the production of furfural from pyrolysis, so far, almost all the studies (e.g. [7]) focused on maximising the dehydration of hemicellulose-rich feedstock (xylose as monomers, $C_5H_{10}O_5$), per **Eq. (1)** below. As hemicellulose only makes up ~15% of a typical lignocellulosic biomass, whilst the other components such as cellulose ($(C_6H_{10}O_5)_n$) can account for 40–45 wt%, the pyrolysis technology for furfural production is far from economically viable. Substantial efforts are thus needed in tailoring the pyrolysis conditions and the design of novel catalysts in maximising the yield and selectivity of furfural from the abundant cellulose within a lignocellulosic biomass.

* Corresponding author.
E-mail address: lian.zhang@monash.edu (L. Zhang).

https://doi.org/10.1016/j.cej.2024.154314
Received 22 April 2024; Received in revised form 27 June 2024; Accepted 25 July 2024
Available online 26 July 2024

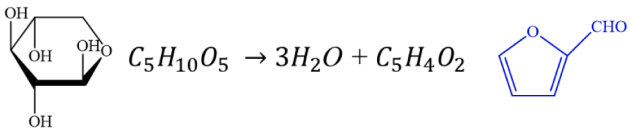

(1)

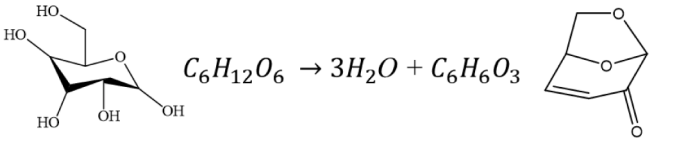

(2)

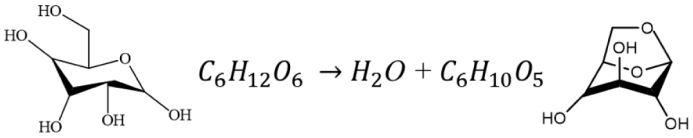

(3)

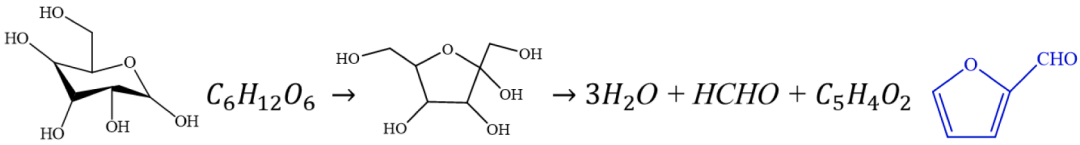

(4)

To date, cellulose (glucose as one of its monomers, $C_6H_{12}O_6$) has been confirmed to mainly undertake dehydration reaction during fast pyrolysis, leading to the production of two principal C6 products, levoglucosenone (LGO, $C_6H_6O_3$) and levoglucosan (LGA, $C_6H_{10}O_5$) per **Eqs. (2) and (3)** above [1,8–10]. To facilitate the production of furfural which is a C5 component, apart from the dehydration reaction, isomerisation and subsequent Grob fragmentation reaction to eliminate the formaldehyde (HCHO) site group (**Eq. (4)**) are essential [11]. However, the study in this attempt is sporadic. Bai et al. [12] reported a Na/Fe-solid acid catalyst that is active in achieving a furfural selectivity of 61.4% from the fast pyrolysis of cellulose at 550 ℃, with the use of a high catalyst to cellulose mass ratio of 10, whilst the mass yield of furfural and the stability of catalysts were not reported. More recently, we reported a Pd-PdO/$ZnSO_4$ bifunctional catalyst with a high furfural yield of 74–82 mol% from the pyrolysis of a variety of C6-rich feedstock, at a typical temperature of 400 ℃ and catalyst to feedstock mass ratio of 8 [11]. Nonetheless, the hydrothermal stability of $ZnSO_4$ during the reaction process remains concerning. Consequently, it is imperative to further fine-tune the catalyst properties such as the use of a more stable support. In addition, there are still a number of unknown research questions to be addressed, including the identification of the Pd-bearing active site, reaction mechanism, and more importantly, assessment of the stability and reusability of the catalyst.

Compared to the highly water-soluble $ZnSO_4$, a mesoporous silica support can offer better mechanical strength, hydrothermal stability, and even other tuneable properties such as pore size that is large enough for the selectivity of a specific product such as furfural with a molecular size of 0.55 nm. For a typical vapor phase derived from the pyrolysis of cellulose to furfural, its glucose monomers, the intermediate LGA and target product furfural have varying kinetic diameters ranging from 0.55 nm to 1.5 nm [13]. As a mesoporous silica support, MCM-41 has been confirmed for a superior activity in dehydrating C5 hemicellulose into furfural [14,15]. Its highly ordered and abundant mesopore (2.5–4.5 nm) structure was also confirmed to promote the shape selectivity of furfural over the other liquid derivatives from hemicellulose [7]. In combining MCM-41 and Pd via a simple loading of PdO (~1 *mol%*), this paper aims to explore the activity of the resultant Pd-laden MCM-41 catalyst for the derivation of furfural from the fast pyrolysis of cellulose. As far as the authors are aware, there is still no study on the application of this catalyst to the pyrolysis of biomass. Instead, it has been partially examined during the hydrogenation of 1-hexene and the dehydrogenation of formic acid [16–19]. Compared to these two applications, the pyrolysis of cellulose is more complicated, and it is also expected to generate plenty of oxygen-bearing species/oxidant such as H_2O on the catalyst surface. As such, the active phase of Pd and its phase transformation, if any, are expected to differ noticeably from the previous hydrogenation/deydrogenation studies. Moreover, we speculate that, on the one hand, the surface hydrophilicity of MCM-41 could be altered by the doping of Pd, which in turn could affect the adsorption/desorprtion of nearly all the oxygenates derived from pyrolysis. On the other hand, this combination is expected to be bifunctional for both dehydration and Grob fragmentation to cleave and oxidise formaldehyde. The noble metal catalysts including Pd are even highly active for the oxidation of formaldehyde at room temperature [20,21]. Nevertheless, the phase stability of Pd during the high-temperature pyrolysis of cellulose is still unknown.

Herein, a micro-reactor, namely Pyro-probe coupled with a variety of real-time gas and liquid detectors was employed to test the catalysts. A relatively larger fixed-bed reactor, xylan and real biomass (i.e. wet sugarcane bagasse) was further used to validate the results from Pyro-probe micro-reactor. Various advanced characterisation methods were implemented to explore both bulk and surface properties of the catalyst, whilst the active site and the underpinning mechanism were examined via synchrotron high-temperature in-situ XRD and DRIFTS. Finally, cyclic tests and regeneration of the spent catalyst via air combustion were performed to test the stability and reusability of the catalyst, as well as to further provide insights on the reconstruction of the Pd-bearing active site upon the alternation of reaction and regeneration. These detailed studies are beneficial in advancing the furfural production from biomass, and the underpinning knowledge governing the activity of the Pd-centered site and its strong metal-support interaction with MCM-41 that are yet to be understood under the typical high-temperature biomass upgrading conditions.

2. Experimental

2.1. Materials

A variety of feedstocks and chemicals were explored, including cellulose (Sigma-Aldrich, product number: 435363, the particle size of 51 μm), xylan from corn core (TCI America, product number: X0078), LGO ($C_6H_6O_3$, Sigma-Aldrich, product number: SMB00504), LGA ($C_6H_{10}O_5$, Sigma-Aldrich, product number: 06724), 5-HMF ($C_6H_6O_3$, Sigma-Aldrich, product number: H40807), furfural ($C_5H_4O_2$, Sigma-Aldrich,

Table 1
Physiochemical properties of the Pd-MCM-41 catalyst (fresh, spent, and regenerated) with 1 mol% Pd.

		Pd ratio, mol%	Porosity analysis			Acidity, by NH_3-TPD (mmol/g)				B/L[d], by Pyridine-FTIR	Crystalline size[e], (nm)	TEM particle size, (nm)
			S_{BET}[a], (m^2/g)	V_p[b], (cm^3/g)	Dp[c], (nm)	Weak (<200 °C)	Medium (200–600 °C)	Strong (600–800 °C)	Total			
Fresh	PdO	100	2	0.0028	5.5	0	0	4.48	4.48	0.024	–	–
	MCM-41	0	907	0.93	3.7	0.11	0.01	–	0.12	0.023	–	–
	Pd-MCM-41	1*	830	0.84	3.5	0.14	0.04	–	0.18	0.028	8.1	4.5
Spent	MCM-41	0	624	0.42	2.9	–	–	–	–	–		
	Pd-MCM-41	1	683	0.57	3.0	–	–	–	–	–	10.3	6.2
Regenerated Pd-MCM-41		1	785	0.76	3.7	–	–	–	–	–	9.1	5.3

*Determined by ICP-MS;
a-BET specific surface area;
b-Total pore volume estimated at P/P0 = 0.99;
c-Average pore size, 4 V/A by BET;
d-Brønsted acid/Lewis acid, semi-quantified by area%;
e-Averaged crystallite size as estimated by the Scherrer equation.

product number: 319910), and formaldehyde solution (HCHO, 37 wt% in water, Sigma-Aldrich, product number: F8775). The chemicals for catalyst synthesis include ethanol (ACS reagent, ≥ 99.5%, absolute), palladium (II) nitrate dihydrate ($Pd(NO_3)_2{\cdot}2H_2O$, ~40% Pd basis, product number: 76070, batch number: BCCL4834), polyvinylpyrrolidone (PVP, M_w = 40000 g/mol, product number: PVP40, batch number: 0000343982), and commercial MCM-41 (SiO_2, product number: 643645, batch number: BCCK7273) were also purchased from Sigma-Aldrich. The gases used include helium (He, 99.999%), 5% H_2 in N_2, 1% H_2 in N_2, and 1% CO in N_2 purchased from BOC Australia.

2.2. Synthesis of Pd-MCM-41 catalysts

The Pd-MCM-41 catalysts were synthesised using the ligand assisted impregnation method, per the literature [22,23]. MCM-41 was pretreated at 500 °C in air for 2 h. PVP ($(C_6H_9NO)_n$) was used as the ligand, which is one of the most common ligands for preparing metal nanoparticles with high dispersion and minimal agglomeration [23]. Firstly, 0.0274 g of $Pd(NO_3)_2{\cdot}2H_2O$ and 0.274 g of PVP were mixed and dispersed in 30 mL ethanol (ACS reagent, ≥ 99.5%, absolute) with a continual stirring and sonication in 30 min. Secondly, 0.548 g MCM-41 was added into the mixture, stirred and sonicated twice for 1 h, followed by being placed overnight (without stirring) under the ambient conditions to ensure a thorough impregnation of the support with Pd species. Thirdly, the mixture was filtered and oven-dried at 80 ℃ for 12 h, and finally, the solid was calcined at 500 ℃ at a heating rate of 1 ℃/min and then held for 2 h in air. The nominal loading of Pd was varied between 0 and 10 mol%. For comparison, a pure PdO catalyst was prepared by simply calcining $Pd(NO_3)_2{\cdot}2H_2O$ at 500 ℃. To explore the catalytic role of metallic Pd^0, the fresh Pd-MCM-41 with 1 mol% Pd was purposely reduced in 5% H_2 at 400 ℃ for 2 h, and the obtained catalyst was named rPd-MCM-41.

2.3. Catalyst characterisation

The fresh, spent, and regenerated catalysts were characterised by a number of bench-top analytical instruments, including X-ray powder diffraction (XRD); X-ray photoelectron spectroscopy (XPS); Brunauer-Emmett-Teller (BET) surface analysis; high-resolution transmission electron microscopy (HRTEM); scanning electron microscopy (SEM) on a JEOL 7001F FEGSEM – BH equipped with back-scattered electron (BSE) detectors; ammonia-temperature programmed desorption (NH_3-TPD) for acidity; CO-pulse chemisorption for metal dispersion; Pyridine-FTIR for the Brønsted (B) and Lewis (L) acidic sites; ICP-MS for elemental composition; and CHNS analyser to quantify the content of coke. In addition, the catalysts were subjected to synchrotron high-temperature XRD (HT-XRD) and X-ray absorption spectroscopy (XAS) analysis. Detailed conditions for each analysis can be found in Section 4 of **SI**.

2.4. Fast pyrolysis experiments

The fast pyrolysis experiments were carried out on a Pyro-probe microreactor (CDS 5200) coupled with a GC-TCD/FID/MS (Agilent 7890B) detector. As in **Fig. S1**, the quartz reactor was loaded with feedstock in the front, whilst the catalyst was placed after it. Quartz wool was also placed between feedstock and catalyst to separate them, whereas the pyrolysis vapor from biomass was entrained by the carrier gas (>99.999% He, 26 mL/min) to flow through the catalyst. The reactor was surrounded by a Pt-filament with an estimated particle heating rate of ~150 ℃/s within the quartz reactor, according to COMSOL simulation results reported elsewhere [24]. The amount of feedstock in each experiment was fixed at around 0.5 mg, whereas the mass of the catalyst was varied at different mass ratios of 1–4 to the feedstock. Apart from the dried feedstock, the wet feedstock with varying amounts of water added was also tested. This is to mimic the wet biomass, e.g. bagasse, that can contain up to 45–50 wt% moisture [25]. The pyrolysis temperature was set at 350–550 ℃ for a duration of 25 s at each temperature. At least three repetitions were conducted for each condition. The mass balance calculation results in **Section 3.1** of **SI** verified the high accuracy of the Pyro-probe system.

The total yield of gas and liquid (%) was defined as the difference of the original mass of cellulose (dry-and-ash free) to the residue, per **Eq. (5)** below. For the yields of individual non-condensable gases, including H_2, CO_2, C_2H_4, C_2H_6, CH_4, and CO, and H_2O, they were detected and quantified via a TCD detector with a Molseive column and a Hayesep Q column. Standard gases were used for the calibration of individual gases, as detailed in **Section 3.2** of **SI**. Accordingly, the sum of the yields for these gases was defined as the yield of the total non-condensable gas. Consequently, the yield of total liquid (i.e., condensable organic vapors without the inclusion of water) was defined as the difference between the overall conversion of cellulose and total gas yield, per **Eq. (6)** blow. Finally, regarding the liquid products, they were analysed by an online

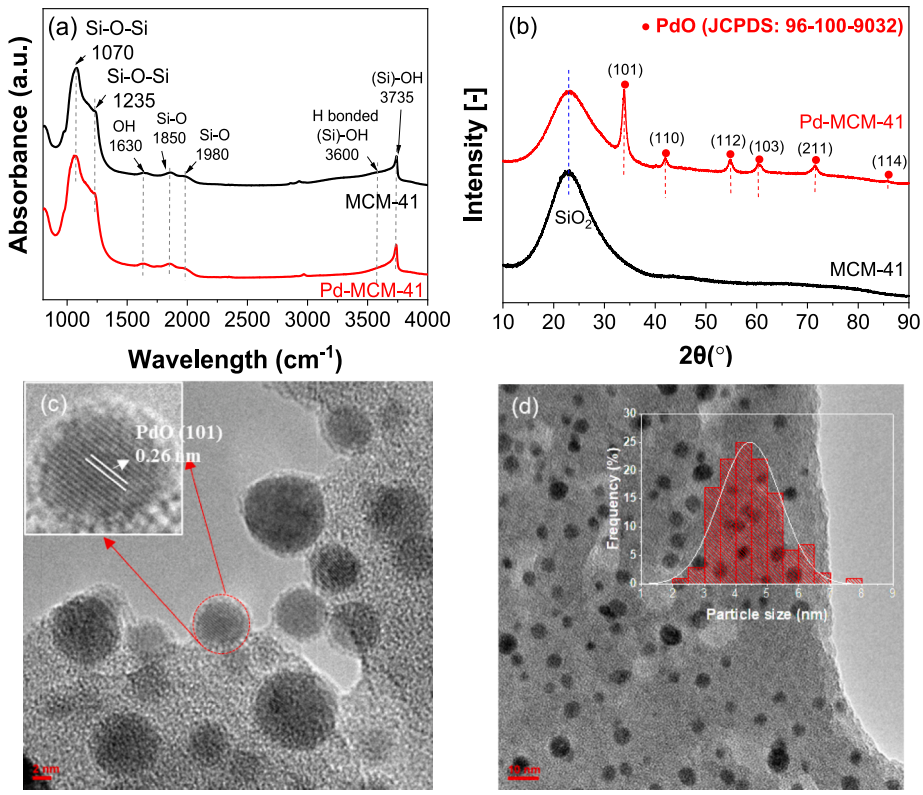

Fig. 1. (a) Surface functional group of fresh MCM-41 and Pd-MCM-41 catalysts; (b) XRD patterns of fresh Pd-MCM-41 and MCM-41 catalysts; (c-d) HRTEM and typical TEM patterns of fresh Pd-MCM-41 catalyst with its particle size distribution calculated per the counting of 122 particles.

MS detector with a capillary column (HP-5MS). The chromatographic peaks in MS spectra were summarised in Table S1. The selectivity of our target product furfural was calculated based on the peak area ratio in the GC–MS spectra, per **Eq.** (7). To quantify the mass yield of furfural, we further calibrated the furfural peak area upon the use of known concentrations of furfural in furan solvent, as shown in **Eq. (S7)** with details in Section 3.3 of **SI** and our previous work [11]. Afterwards, based on the total liquid yield and furfural mass concentration, we determined the furfural mass yield per **Eq.** (8).

$$\textit{Total yield of gas and liquid}\ (\%) = \frac{\textit{Mass of cellulose} - \textit{mass of residual solid} - \textit{mass of } H_2O}{\textit{Mass of cellulose}} \times 100\% \quad (5)$$

$$\textit{Yield of liquid}\ (wt\%) = \textit{Total of gas and liquid} - \textit{yield of total gas} \quad (6)$$

$$\textit{Selectivity of furfural}\ (\%) = \frac{\textit{Area of furfural}}{\textit{Area of all compounds}} \times 100\% \quad (7)$$

$$\textit{Yield of furfural}\ (wt\%) = \textit{Yield of liquid} \times \textit{furfural mass concentration} \quad (8)$$

To further corroborate the catalytic activity, pyrolysis of cellulose, xylan, and sugarcane bagasse were conducted in a relatively large fixed-bed reactor, as detailed in Section 3.4 of **SI**. In brief, for each run, approximately 0.5 g feedstock was loaded into a crucible with and without the same quantity of catalyst on the top of the feedstock. The furnace was pre-heated to a set temperature; the feedstock-laden crucible was then quickly inserted into the hot furnace and kept on hold for 30 min, and the resultant vapor passed through an impinger train for collection. Finally, the liquid condensate was analysed by a GC–MS (DB-5MS column) offline. The averaged heating rate, as determined from the measured temperature of the crucible inside the hot furnace, is around 30 ℃/min. The gas residence time is around 70 s through the entire quartz reactor.

2.5. *In-situ reflectance infrared Fourier transform spectroscopic measurement (in-situ DRIFTS)*

To explore the surface hydrophobicity of catalyst and the adsorption/desorption of the species of interest on the catalyst surface, in-situ DRIFTS measurement was conducted upon the flow of a variety of molecules, including water vapor, HCHO, and furfural through the catalyst surface. Furthermore, to capture the probable phase change of Pd, temperature-programmed reduction (TPR) of Pd-MCM-41 in HCHO, H_2, or CO was also examined using in-situ DRIFTS. The detailed measurement conditions are presented in **Section 3.5** of **SI**.

3. Results and discussion

3.1. *Properties of fresh catalyst with 1 mol% Pd*

For a typical fresh Pd-MCM-41 catalyst with 1 mol% Pd (which is also the optimum Pd quantity, as detailed later), its physicochemical properties, along with two references, pure PdO and blank MCM-41 are shown in Table 1. The respective result of Pd quantification and the

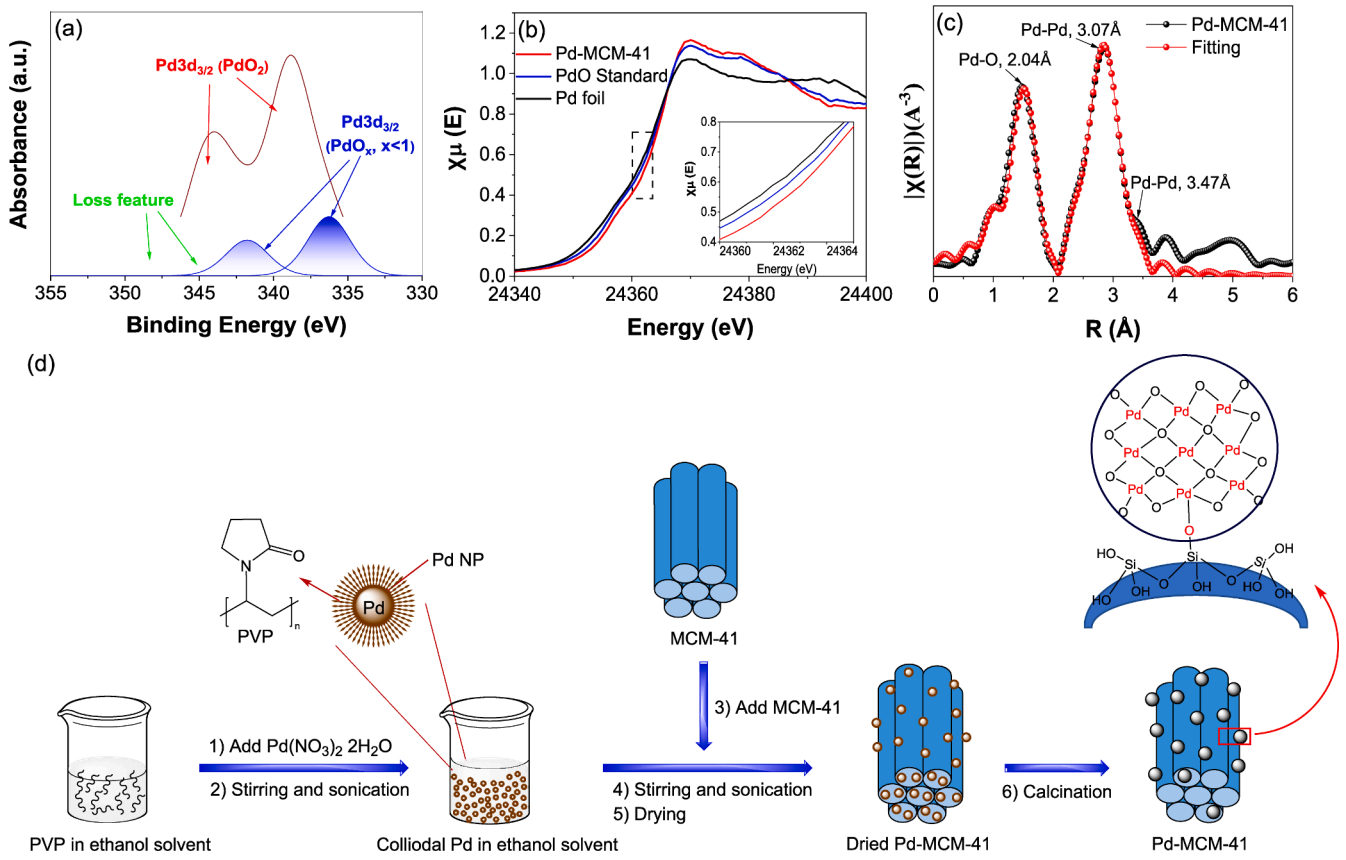

Fig. 2. (a) XPS Pd $3d_{3/2}$ spectrum for Pd-MCM-41 catalyst with 1 mol% Pd; (b) Pd K-edge XANES spectra for Pd-MCM-41 catalyst, PdO standard, and Pd foil; (c) Pd K-edge EXAFS fitting spectra for Pd-MCM-41, shown in R-space; (d) proposed synthesis of fresh Pd-MCM-41 catalyst.

patterns of BET, NH_3-TPD, and Pyridine-FTIR can be found in **Figs. S2-S3**. As in Table 1, the MCM-41 reference has a large specific surface area of 907 m^2/g, a pore volume of 0.93 cm^3/g, and an average pore size of 3.7 nm, all of which are for a typical mesoporous structure [26]. Upon the doping of 1 mol% Pd, the specific surface area and pore volume for the resultant Pd-MCM-41 catalyst slightly dropped to 830 m^2/g and 0.84 cm^3/g, respectively. Presumably, the majority of Pd reside on the outside of the MCM-41 matrix. Indeed, **Fig. S2** show similar patterns between Pd-MCM-41 and blank MCM-41 both in specific surface area and pore size distribution. The CO-impulse measurement also confirmed a surface dispersion of 48% for Pd. Regarding the surface acidity in Table 1, the pure PdO reference has the strongest acidity at 600–800 ℃, while MCM-41 has a relatively weak acidity < 200 ℃, and a negligible medium acidity at 200–400 ℃. The doping of 1 mol% Pd slightly increased the strength for both weak and medium acids, and the the resultant Brønsted to Lewis acid (B/L) ratio.

Fig. 1**(a)** show a similar pattern between Pd-MCM-41 and blank MCM-41 in surface functional group distribution. XRD patterns in Fig. 1 **(b)** show a broad lump at $2\theta = 23.9°$ for MCM-41 reference reflecting the amorphous nature of the pore wall within the MCM-41 matrix [27,28]. As expected, the pure PdO reference (**Fig. S4(a)**) is fully consistent with the standard oxide (JCPDS: 96-100-9032). Regarding Pd-MCM-41, the most discernible peak is for the (1 0 1) plane of PdO oxide, followed by tiny ones including (1 1 0), (1 1 2), (1 0 3), (2 1 1), and (1 1 4). This agrees with the HRTEM images (Fig. 1**(c)**) for the presence of spherical PdO nanoparticles with a featuring d-space of 0.26 nm for its (1 0 1) facet. Furthermore, per the Scherrer equation, the formed PdO particles on Pd-MCM-41 are estimated to have a crystallite size of ~8.1 nm, broadly agreeing with the averaged PdO particle size of ~4.5 nm per HRTEM observation in Fig. 1**(c)** and Fig. 1**(d)**. As this is larger than the average pore size of ~3.7 nm in MCM-41, it is confirmed that the loaded Pd mostly resides on the outer wall of the support.

Fig. 2**(a)** for the XPS Pd 3d analysis of catalyst surface shows the primary existence of 77.2% Pd as $Pd^{4+}O_2$, along with a small fraction of 22.8% as PdO_x ($0 < x < 1$). This broadly agrees with Fig. 2**(b)** for the XANES profile of bulk Pd K-edge, where the Pd-MCM-41 shows a blue-shift towards higher absorption energy for a higher oxidation valance. This shall be caused by the chelation of the original Pd^{2+} by the PVP ligand. The abundant oxygen molecules within PVP are in favour of the oxidation of Pd^{2+}. The Fourier transferred EXAFS spectra in Fig. 2**(c)** and **Fig. S5**, along with the corresponding fitting results detailed in **Table S2**, confirmed a Pd-O bond length of 2.04 Å and coordination number of 5 for the first shell, which is respectively slightly different from the standard length of 2.01 Å and coordination number of 4 for the pure $Pd^{2+}O$ [29]. For the second shell, the Pd-Pd bond length is 3.07 Å, also deviating from the pure $Pd^{2+}O$ standard length of 3.02 Å. Finally, based on all the characterisation results, the corresponding synthesis of loading Pd on MCM-41 is proposed in Fig. 2**(d)**, where Pd colloid is expected to be formed during the PVP chelation stage [22], promoting a highly dispersed Pd species on the MCM-41 support, as proved by the BET and TEM results for the dried Pd-MCM-41 prior to calcination in **Fig. S6**. The subsequent calcination removed the abundant nitrogen (N) and carbon (C) within the PVP (as confirmed by the CHNS result in **Table S3**), causing the growth of the Pd nanoparticles into larger clusters that are mostly excluded out of the MCM-41 matrix.

3.2. Catalytic performance of Pd-MCM-41

3.2.1. Product distribution from dried cellulose pyrolysis

Fig. 3 shows the product distribution from the pyrolysis of dried cellulose at 450 ℃, upon the use of different catalysts with an equal mass ratio of catalyst to cellulose. Note that the Pd content was fixed at 1 mol

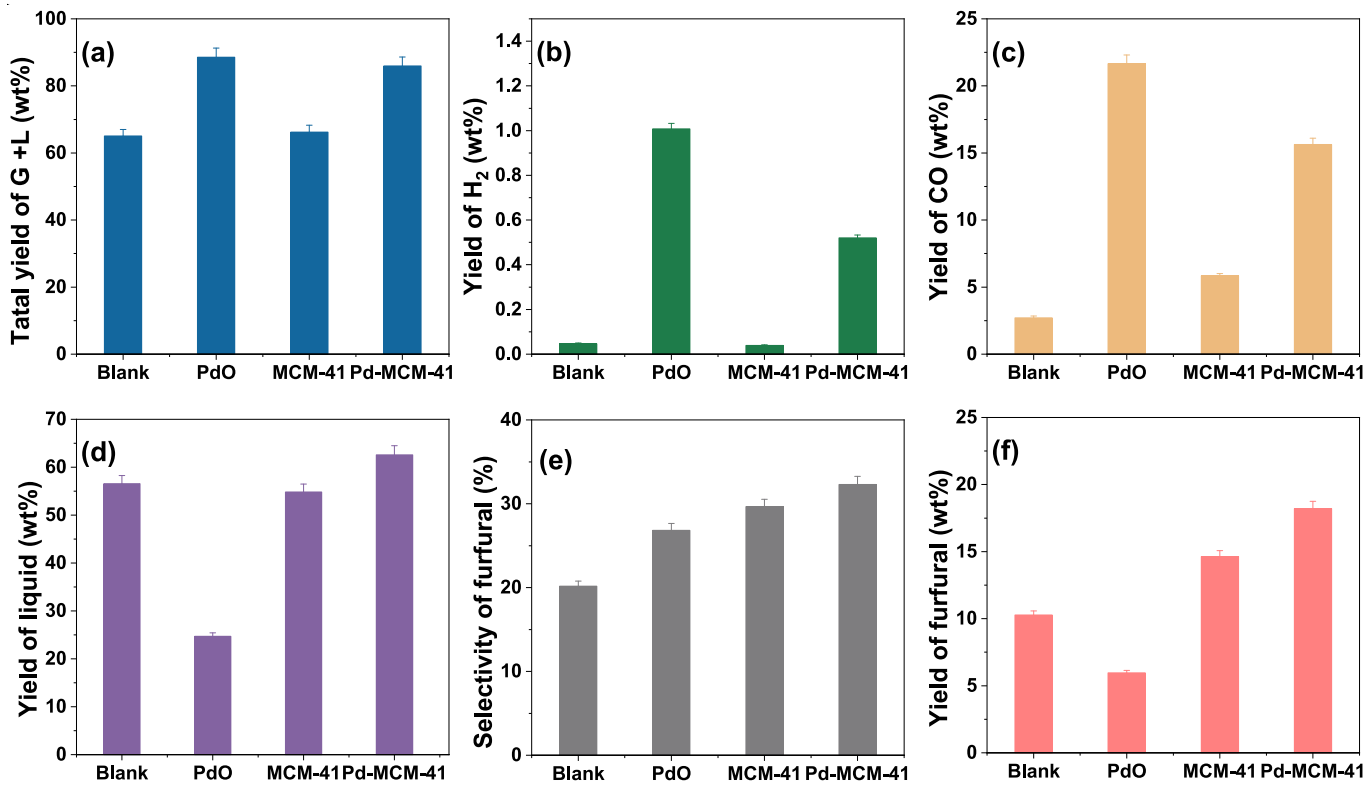

Fig. 3. Products distribution from dried cellulose fast pyrolysis at 450 ℃ with and without the use of catalysts at an equal mass ratio to cellulose. (a) Total yield of Gas (G) and Liquid (L); (b) H_2 yield; (c) CO yield; (d) Liquid yield; (e) Furfural selectivity; and (f) Furfural yield. Note that the content of Pd is 1 mol% in the Pd-MCM-41 catalyst.

% in the Pd-MCM-41 catalyst. The corresponding GC–MS spectra are shown in **Fig. S7**, and the detailed results are listed in **Table S4**. As in Fig. 3**(a)**, over the blank MCM-41, the total yield of gas and liquid out of cellulose reached ~68 wt%, which is similar with the blank case of cellulose alone. For the pure PdO reference, the total yield of gas and liquid reached ~89 wt%, due to the strongest cracking of the C-C bonds in the sugar rings. In contrast, the use of Pd-MCM-41 can achieve a comparably high total yield of gas and liquid with its pure PdO counterpart (Fig. 3**(a)**), whilst the formation of permanent gases was greatly suppressed. As in Fig. 3**(b)-(c)**, the pure PdO led to a high H_2 yield of ~1.0 wt% and CO of ~21.7 wt%, which is also accompanied by ~41.2 wt% CO_2 (**Table S4**). In contrast, the gas product from Pd-MCM-41 mainly consists of H_2 and CO, and the CO_2 yield is only ~6.8 wt%. Accordingly, the highest liquid yield is obtained over the Pd-MCM-41 catalyst, as shown in Fig. 3**(d)**.

For the furfural selectivity and yield in Fig. 3**(e)-(f)**, clearly, the pure PdO was able to selectively cleave the unwanted species, thereby increasing the furfural selectivity. Nevertheless, its over-cracking activity deteriorated the overall liquid amount, thereby leading to the least furfural yield. The use of MCM-41 alone led to an improved furfural selectivity of ~29.6%. However, the selectivity of other compounds, including LGO is also remarkably high, as evident in **Table S4** and **Fig. S7**. These products can be formed simply by the dehydration of cellulose over MCM-41 [30,31], as illustrated in **Eq. (2)**. Notably, the Pd-MCM-41 catalyst achieved the highest selectivity and yield of furfural with ~32.3% and ~18.2 wt%, respectively, while the selectivity of heavy compounds decreases sharply (**Table S4**). Following this, a parametric examination was conducted to optimise the loading of Pd, mass ratio of catalyst to cellulose, and reaction temperature. As in **Fig. S8**, the results confirmed that 1 mol% is the best Pd loading percentage, 450 ℃ is the optimum temperature, whilst an equal mass ratio of catalyst to cellulose is sufficient for the Pd-MCM-41 catalyst developed here. These conditions were used to further test the pyrolysis of wet cellulose in the following section.

3.2.2. *Effect of water addition (wet cellulose) on product distribution*

The results for wet cellulose are summarised in Fig. 4**(a)-(d)** and the corresponding GC–MS spectra for liquid species are in **Fig. S9**. Note that the drying curve of cellulose with various moisture contents in **Fig. S10** suggested an approximate 4–5 s delay upon a three-times increase on the

Table 2
Furfural selectivity and yield from fast pyrolysis of cellulose, xylan and sugarcane bagasse in a fixed-bed reactor.

	Dry cellulose[a]	Wet cellulose[a,b]	With Pd-MCM-41[c]					
			Wet cellulose[b]				Wet xylan[b]	Wet sugarcane bagasse[d]
	450 ℃	450 ℃	400 ℃	450 ℃	500 ℃	550 ℃	450 ℃	450 ℃
$S_{furfural}$, %	8.1	19.3	22.2	47.5	43.0	40.4	65.4	35.1
$Y_{furfural}$, wt%	6.2	13.9	13.8	31.3	25.8	18.6	44.5	23.9

[a]without catalyst;
[b]Mass ratio of 3 for water to feedstock;
[c]An equi-mass ratio of catalyst to feedstock;
[d]50% moisture based on the mass of sugarcane bagasse.

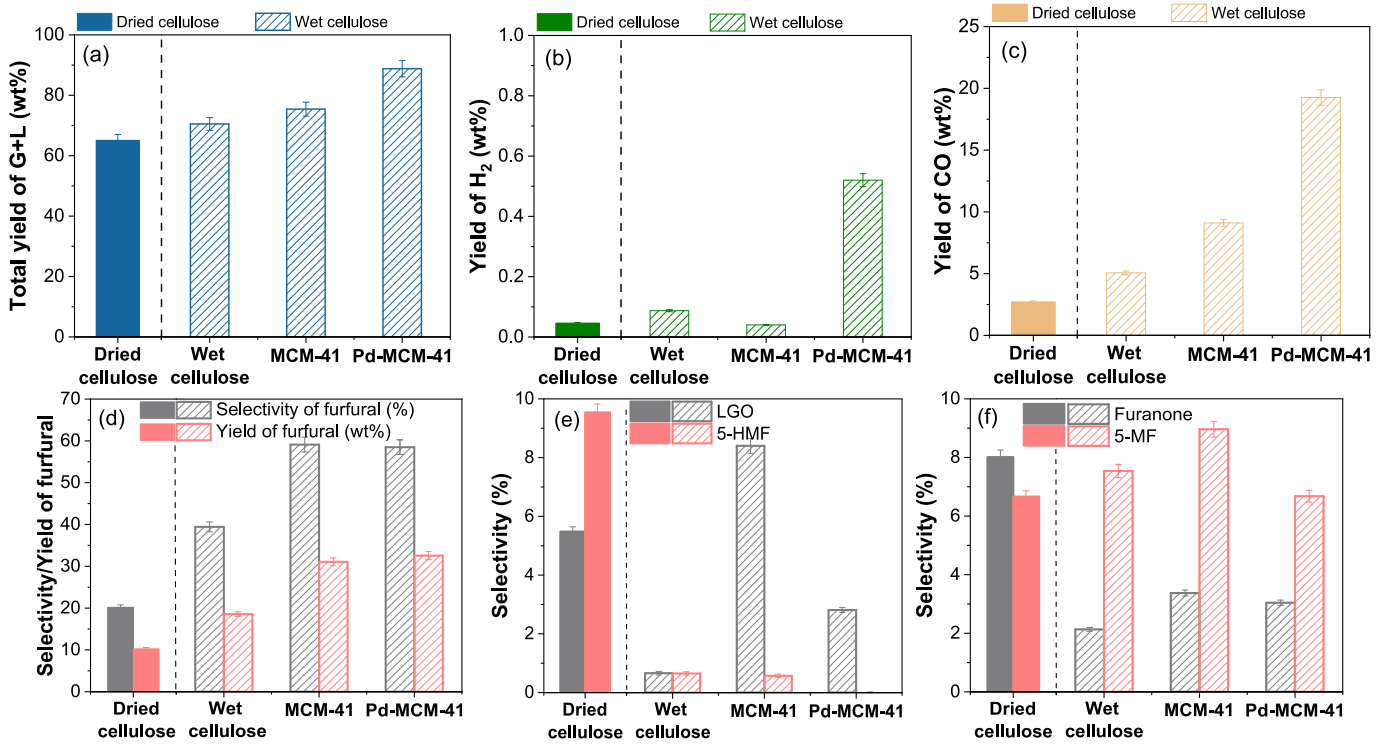

Fig. 4. Products distribution from wet cellulose pyrolysis at 450 ℃ over different catalysts at an equal mass ratio of catalyst to cellulose for (a) total yield of gas (G) and liquid (L); (b) H_2 yield; (c) CO yield; (d) furfural selectivity and yield; (e) LGO and 5-HMF selectivity; and (f) Furanone and 5-MF selectivity. Note that the cases of dried cellulose and wet cellulose are without the use of catalyst.

Table 3
Furfural selectivity from the pyrolysis of cellulose in Pyro-probe reactor.

Catalysts	Reaction conditions	$S_{furfural}$ (%)[a], $Y_{furfural}$ (wt%)[b]	Reference, years
Pd-MCM-41	450 ℃, 25 s, $R^c = 1$	58.5%, 32.5 wt%	This work
Pd-PdO/$ZnSO_4$	400 ℃, 25 s, $R^c = 8$	55.4%, 33.7 wt%	[11], 2023 (Our previous work)
WO_3/γ-Al_2O_3	600 ℃, 15 s, $R^c = 4$	13.4%	[36], 2022
Cd-MCM-41	550 ℃, 15 s, $R^c = 5$	23.9%	[37], 2021
Impregnated with 2.75% H_2SO_4	300 ℃, 20 s	6.6%, 2 wt%	[38], 2020
$Na/FeCl_3$	550 ℃, 15 s, $R^c = 10$	61.4%	[12], 2019
MCM-41	650 ℃, 18 s, $R^c = 9$	18.5%	[39], 2018
ZrCu-SAPO-18	600 ℃, 15 s, $R^c = 8$	27.6%	[40], 2018
GaN	550 ℃, 10 s, $R^c = 2$	23%	[41], 2017

[a] $S_{furfural}$ (%) represents selectivity of furfural (%);
[b] $Y_{furfural}$ (wt%) represents yield of furfural (wt%);
[c] R stands for the mass ratio of catalyst to feedstock.

moisture content [32]. Such a delay should be insignificant in comparison to the total 25 s residence time within the micro-reactor.

Regarding the total yield of gas and liquid out of wet cellulose in Fig. 4**(a)**, it is evident that the Pd-MCM-41 catalyst is still highly active, which increased the overall conversion of wet cellulose to around 90%. This is accompanied by a remarkable increase in both H_2 and CO in Fig. 4**(b) and (c)**, respectively, compared to wet cellulose without a catalyst. In addition, as the yield of the undesired CO_2 remained rather stable in **Table S5**, it is inferred that, instead of decarboxylation of cellulose, the secondary reactions such as steam reforming or the decomposition of aldehyde (which is formaldehyde here) or ketone-type compounds [33] was promoted by the Pd-MCM-41 catalyst. More importantly, as in Fig. 4**(d)**, using MCM-41 with and without the loading of Pd, both the selectivity and yield of our target product furfural were improved remarkably. This indicates a strong promotion effect of water on the production of furfural. However, in terms of other liquid products in Fig. 4**(e) and (f)**, in comparison to MCM-41 alone, the use of Pd-MCM-41 is clearly beneficial in surpassing the production of LGO, 5-HMF, and furanone. As the yields of H_2 and CO are the highest for this catalyst in Fig. 4**(b) and (c)**, here again, it is inferred that these undesired species were successfully steam-reformed by the Pd-MCM-41 catalyst. In addition, we found that a further increase of the water mass ratio to 4 is detrimental (as shown in **Fig. S11**), which reduced the furfural yield and selectivity considerably. This shall be due to the enhanced steam reforming reaction for furfural leading to the formation of excessive light compounds.

Finally, the catalytic activity of Pd-MCM-41 was validated by the fixed-bed reactor, under the optimised conditions of an equal mass ratio of catalyst to cellulose, a threefold mass ratio of water to cellulose, and a pyrolysis temperature of 450 ℃. Intriguingly, as summarised in Table 2,

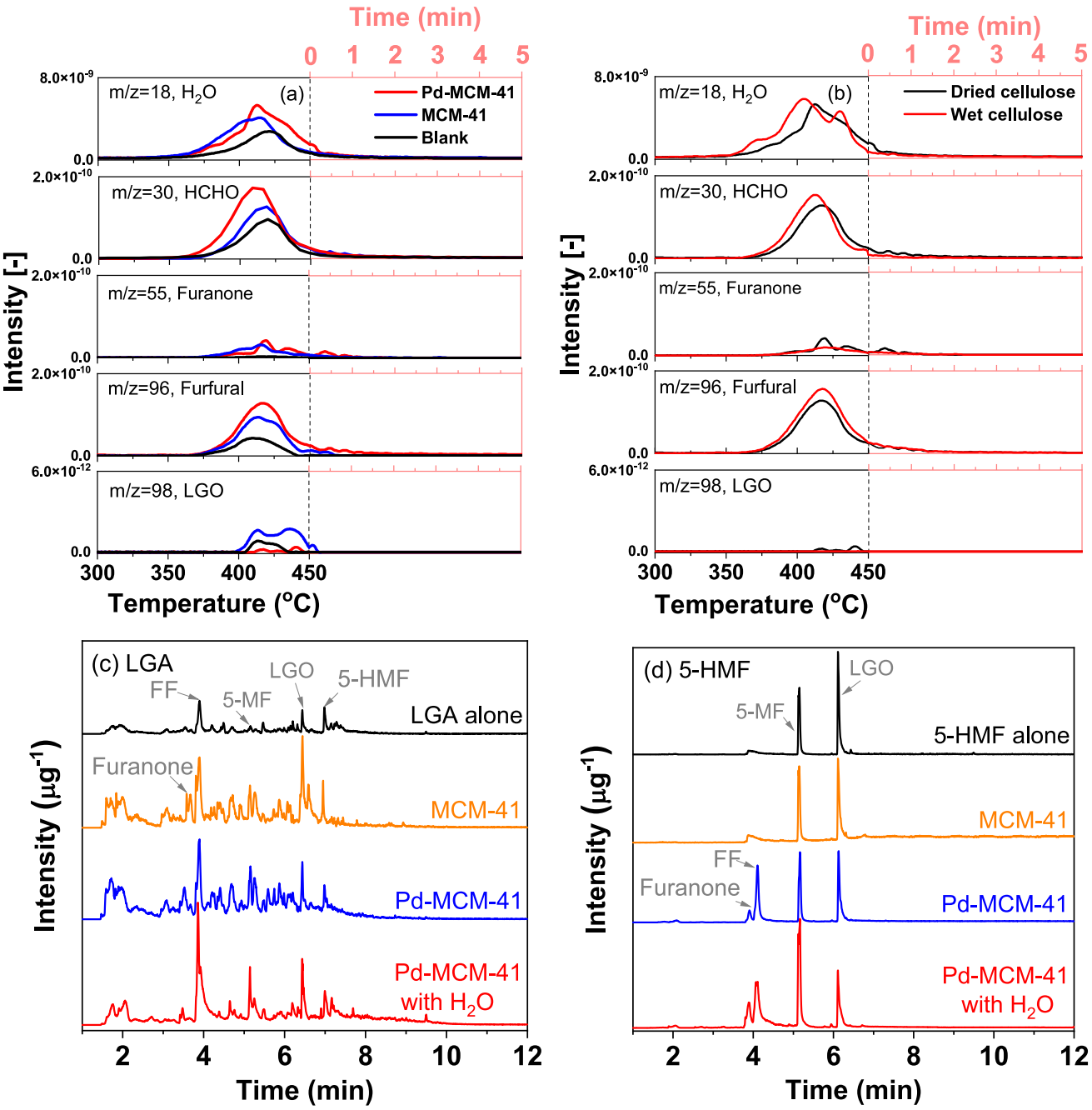

Fig. 5. TGA-MS evolution profiles of individual products at m/z = 18, 30, 55, 96, and 98. Panel (a) for pyrolysis of dried cellulose over different catalysts and (b) pyrolysis of dried cellulose and wet cellulose over the Pd-MCM-41 catalyst from 300 ℃ to 450 ℃ and further hold for 5 min at 450 ℃; (c) for the GC–MS spectra of liquid products from the fast pyrolysis of LGA in Pyro-probe; and (d) for fast-pyrolysis of 5-HMF over different catalysts in Pyro-probe. The conditions for Pyro-probe were set at 450 ℃ and an equi-mass ratio of catalyst to feedstock and a water content of 3 times for panels (c) and (d). For Panels (a) and (b), the scale of Y-axis is set to 8 × 10^{-9} for H_2O, 2 × 10^{-10} for HCHO, furanone, and furfural, and 6 × 10^{-12} for LGO, respectively.

with the detailed product distribution in **Table S6**, and MS spectra in **Fig. S12**, although the heating rate and residence time within the fixed-bed differ from Pyro-probe, the results are quite comparable between the two rigs. The selectivity and yield of furfural are relatively low from dry cellulose pyrolysis, with LGA as the primary product. In the case of wet cellulose, the furfural selectivity and yield were increased, whilst the Pd-MCM-41 catalyst promoted the selectivity and yield of furfural to 47.5% and 31.3 wt%, respectively. These results are comparable with the Pyro-probe data in Fig. 4**(d)**, although LGA was not detected by Pyro-probe. Moreover, our results are superior over those reported based on the solvolysis of cellulose, a conventional commercial approach for furfural production. For instance, based on the use of γ-valerolcatone (GVL)-water as a solvent with a 0.6 wt% $FeCl_3{\cdot}6H_2O$ catalyst at 70 ℃ for 80 min, furfural yield reaches only 14.3 wt% [34]. With the use of γ-butyrolactone (GBL)-water solvent and 1 wt% Hβ zeolite catalyst at 150 ℃, 2 MPa N_2 pressure, and 1 h, the furfural yield only reaches 22.8 wt% [35]. Regarding the pyrolysis method, we also compared our catalyst with those reported based on Pyro-probe. As tabulated in Table 3, the results in this work are clearly comparable with our previous Pd-PdO/$ZnSO_4$ catalyst, and even with the Na/$FeCl_3$ catalyst in terms of furfural selectivity. Additionally, an extra experiment using MCM-41 physically mixed with 1 mol% PdO was conducted at 450 ℃, with an equal mass ratio of catalyst to cellulose and a threefold mass ratio of water to cellulose. As MS spectra shown in

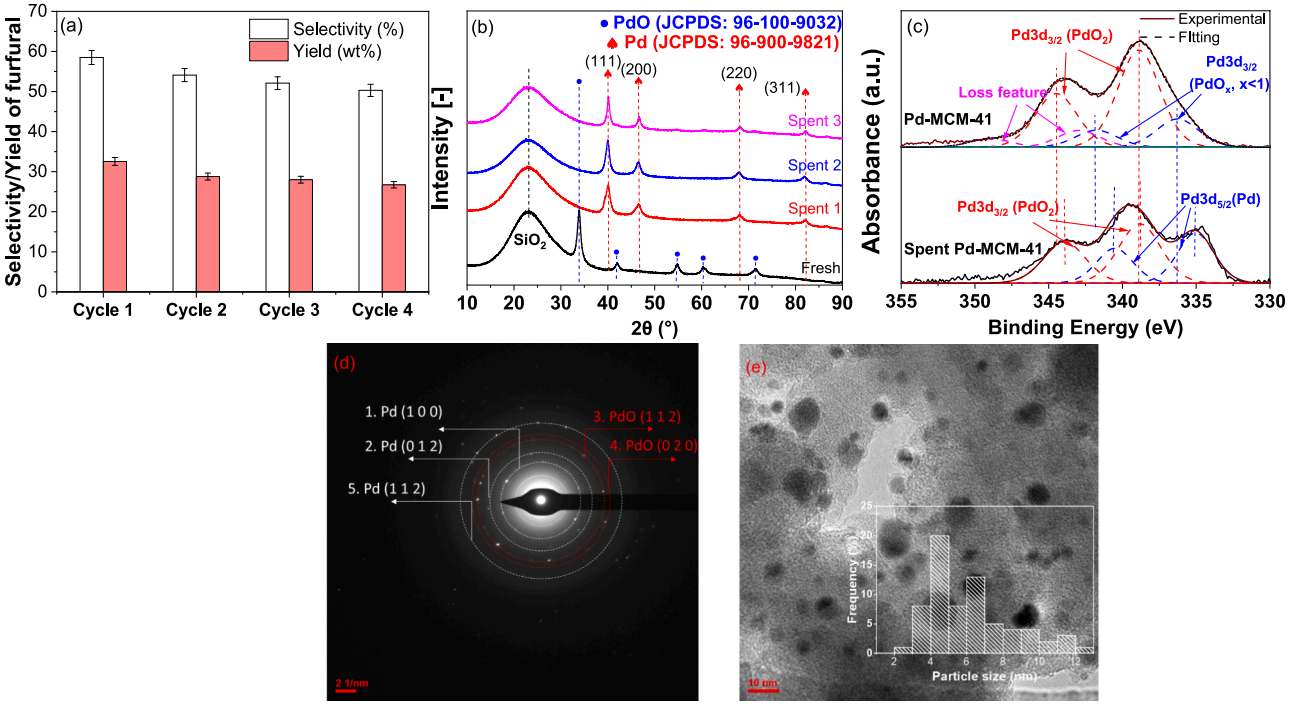

Fig. 6. (a) Selectivity and yield of furfural from the pyrolysis of wet cellulose at different cycle experiments over Pd-MCM-41. The reaction temperature is 450 ℃ and the mass ratio of catalyst to cellulose is set at 1; (b) XRD analysis of the fresh and spent Pd-MCM-41; (c) XPS Pd $3d_{3/2}$ profiles of the fresh and spent Pd-MCM-41 catalysts; (d) TEM electron diffraction pattern and (e) STEM image and particle size distribution of Pd nanoparticles within the spent 1 Pd-MCM-41 catalyst with its particle size distribution calculated per the counting of 70 particles.

Fig. S13, a furfural selectivity and yield of 37.5% and 22.5 wt% were achieved, respectively, confirming the necessity of the impregnation of PdO onto MCM-41. More strikingly, back to Table 2, the catalyst and its optimum application condition can also be successfully extended to the pyrolysis of xylan (i.e., hemicellulose) and a real biomass which is sugarcane bagasse here. For the pyrolysis of wet xylan in fixed-bed reactor, its furfural selectivity and yield reached 65.4% and 44.5 wt%, respectively. Likewise, for the wet sugarcane bagasse, its furfural selectivity and yield achieved 35.1% and 23.9 wt%, respectively. These results even surpass our previous Pd-PdO/$ZnSO_4$ catalyst which yielded 43.8 wt% and 18.3 wt% furfural from the pyrolysis of xylan and sugarcane bagasse, respectively. Moreover, the conditions used in this work are milder than the case for Na/$FeCl_3$ catalyst, which required a higher optimum temperature of 550 ℃ and a larger catalyst to feedstock ratio of 10 [12].

3.3. *Reaction pathways for the evolution of individual products and intermediates*

The time-resolved release of volatile products from slow pyrolysis was analysed by TGA-MS (methods detailed in **Section 3.6**, **SI**), to capture and differentiate the evolution of individual products and intermediate ones that might be missed in the fast-heating scheme. As illustrated for dried cellulose with and without catalysts in Fig. 5**(a), H2O** ($m/z = 18$) is unanimously the first product released at 350 ℃ and peaked at ~400 ℃, echoing the predominance of the dehydration step for the overall conversion (**Eqs. (1)-(4)**). Upon the use of MCM-41 alone, the peak intensity of H_2O increases, along with a peak shift towards lower temperatures. Following this is the release of formaldehyde (HCHO, $m/z = 30$), furfural ($m/z = 96$), furanone ($m/z = 55$), and LGO ($m/z = 98$). The first product is derived from the Grob fragmentation of the methyl side group on the isomerised intermediate D-fructofuranose, per **Eq. (4)**. Its extent was also improved remarkably by the Pd-MCM-41 catalyst. Furthermore, in agreeing with the Pyro-probe results in Fig. 3, the release of furfural and furanone was intensified by this catalyst, whilst the release of LGO was suppressed remarkably in comparison to both the dried cellulose and MCM-41 catalyst. Additionally, LGA was not detected in these cases, which agrees with the Pyro-probe results but differs from the fixed-bed reactor. As LGA is a major anhydromonosaccharide produced from the primary pyrolysis of cellulose [7,42,43], its presence in the fixed-bed derived liquid could be due to a relatively slow heating rate of 30 ℃/min within the fixed-bed reactor. In contrast, higher heating rates of 150 ℃/s and 80 ℃/min were employed in the Pyro-probe reactor and TGA, respectively. Presumably, the dehydration of LGA to LGO was too fast to be captured under these two high heating rates.

Fig. 5**(b)** demonstrates the slow pyrolysis results for both dried and wet cellulose with the use of Pd-MCM-41 catalyst. Clearly, upon the use of wet cellulose, the peaks of H_2O and HCHO further shifted to a lower temperature with enhanced intensity, indicating that both dehydration and Grob fragmentation reactions were promoted. More strikingly, the release of furanone was reduced, whilst the release of LGO was nearly undetectable. This suggests a catalytic conversion of LGO to furfural, or a direct conversion of the precursor of LGO (e.g. LGA) into furfural. To confirm the former speculation, LGO was used as feedstock, blended with and without MCM-41 and Pd-MCM-41 catalysts, and tested at 450 °C and an equal mass ratio of catalyst to feedstock in Pyro-Probe. As evident by the GC–MS spectra of the liquid products in Fig. S14, the LGO intermediate remained intact under all the conditions examined, confirming that it is a competitor to furfural. Once formed, LGO was unable to convert into furfural. In contrast, for the use of LGA as the feedstock in Fig. 5**(c)**, its pyrolysis with the absence of catalysts resulted in a broad range of products from furanone to furfural, 5-MF, LGO, and 5-HMF. However, the use of Pd-MCM-41 improved the selectivity of furfural over LGO, whereas the addition of water further intensified the discrepancy between the selectivity of the two products, making furfural the predominant one. Regarding another principal intermediate 5-HMF formed by dehydration of dried cellulose in Fig. 4, we also used it as a feedstock and tested it with different catalysts. As evident in Fig. 5**(d)**, the use of MCM-41 only is in favour of the isomerisation of 5-HMF into

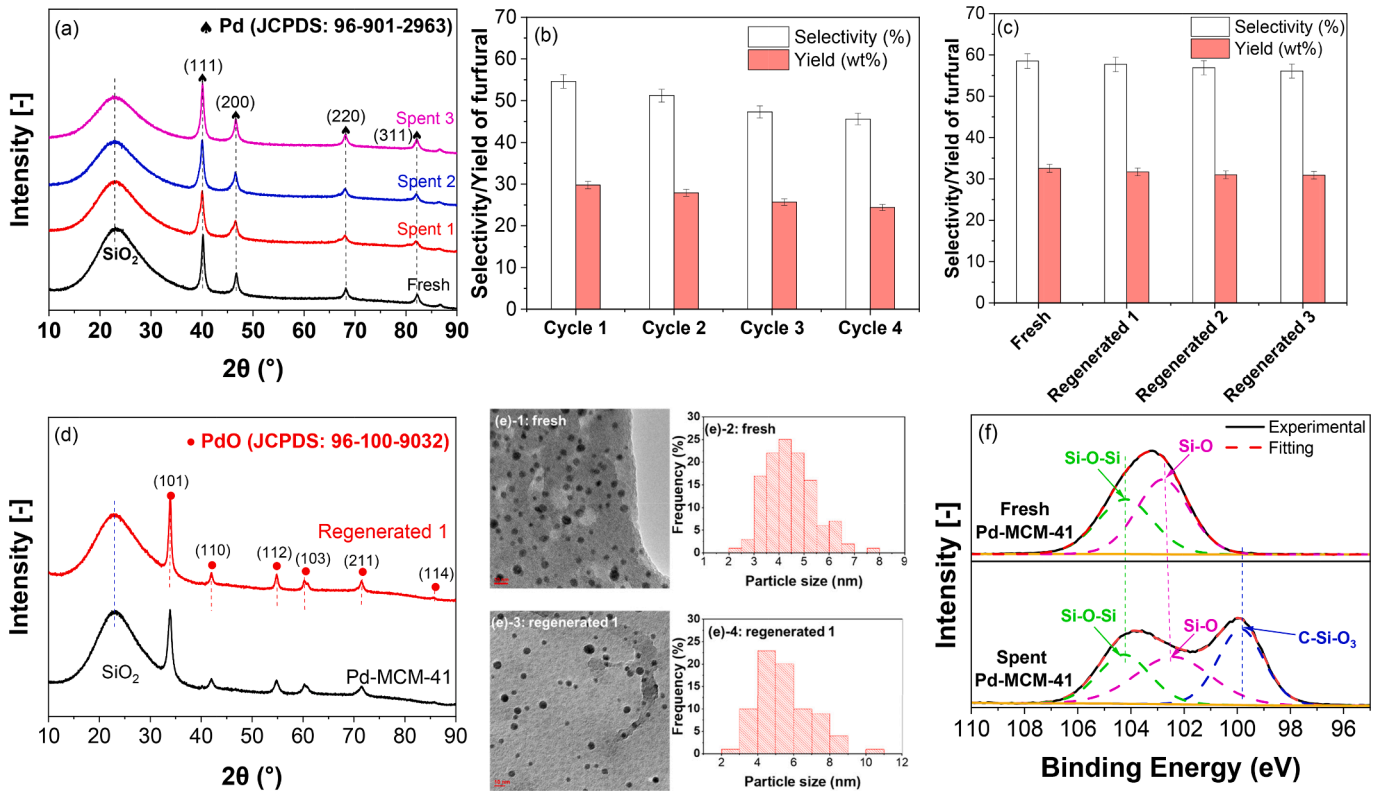

Fig. 7. (a) XRD analysis of fresh and spent rPd-MCM-41; (b) Activity of the H_2-reduced Pd-MCM-41 catalyst, namely rPd-MCM-41 for the selectivity and yield of furfural from the pyrolysis of wet cellulose in different cycles; (c) Activity of regenerated Pd-MCM-41 for three reaction-regeneration cycles. Pyrolysis conditions were fixed at 450 °C and catalyst to cellulose mass ratio of 1; (d) XRD analysis of fresh and regenerated Pd-MCM-41; (e) HRTEM and particle size distribution of: (e)-1 and (e)-2 Pd-MCM-41 catalyst, (e)-3 and (e)-4 regenerated catalyst with its particle size distribution calculated per the counting of 78 particles; (f) XPS Si 2p profiles of the fresh and the spent Pd-MCM-41 catalysts.

LGO, and the hydrogenolysis of 5-HMF into 5-MF. In contrast, the use of Pd-MCM-41 catalyst promoted the formation of both 5-MF and furfural, whilst the addition of extra water reduced the intensity of the LGO competitor. Finally, regarding another light product furanone ($C_4H_4O_2$), it was only detected by fast pyrolysis in Fig. 4**(f)**. Irrespective of the use of a catalyst, the use of wet cellulose is sufficient to reduce the fraction of furanone. This can be due to accelerated hydrolysis of furanone and even its high-temperature decarbonylation reaction [29,44], leading to the formation of CO. Therefore, the combination of MCM-41 and PdO is in favour of both dehydration and Grob fragmentation to remove the undesired HCHO, and more importantly, it is effective in surpassing the undesired LGO and 5-HMF competitors.

3.4. Catalyst active sites and phase change between PdO and Pd^0

3.4.1. Cyclic tests and characterisation of spent Pd-MCM-41 catalyst

Effort was then made to assess the reusability of the spent Pd-MCM-41 and its characteristics post each single test. As in Fig. 6**(a)**, a steady decrease was confirmed for the cyclic tests on both yield and selectivity of furfural (GC–MS spectra in **Fig. S15**). For comparison, the MCM-41 support alone also demonstrated a descending trend with a much faster decrease rate upon the increase on the cycle number (**Fig. S16**). The CHNS results in **Table S7** and BET pore distribution in **Fig. S17** of the spent catalysts indicated a larger quantity of coke deposition on the spent MCM-41 than the spent Pd-MCM-41, underscoring the detrimental role of coke on the deactivation of MCM-41 with and without the loading of Pd. Additionally, in parallel to the coke deposition on Pd-MCM-41, the phase change of Pd was also found. As in Fig. 6**(b)**, the

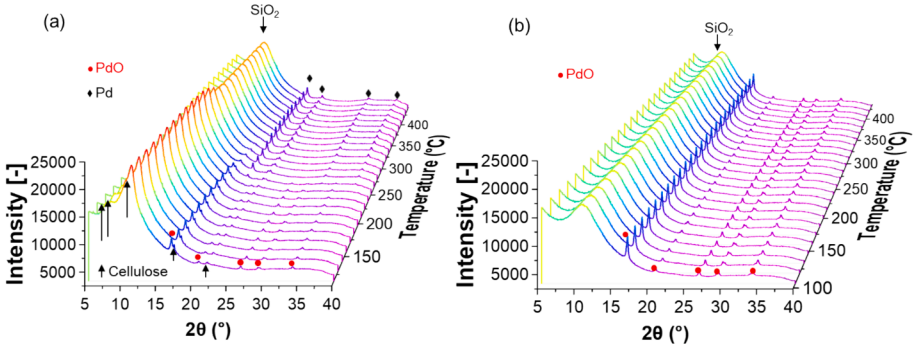

Fig. 8. In-situ XRD analysis of (a) Pd-MCM-41 mixed with cellulose and (b) fresh Pd-MCM-41 catalyst during temperature-programmed heating from 100 °C to 450 °C in N_2. The heating rate was set at 10 ℃/min.

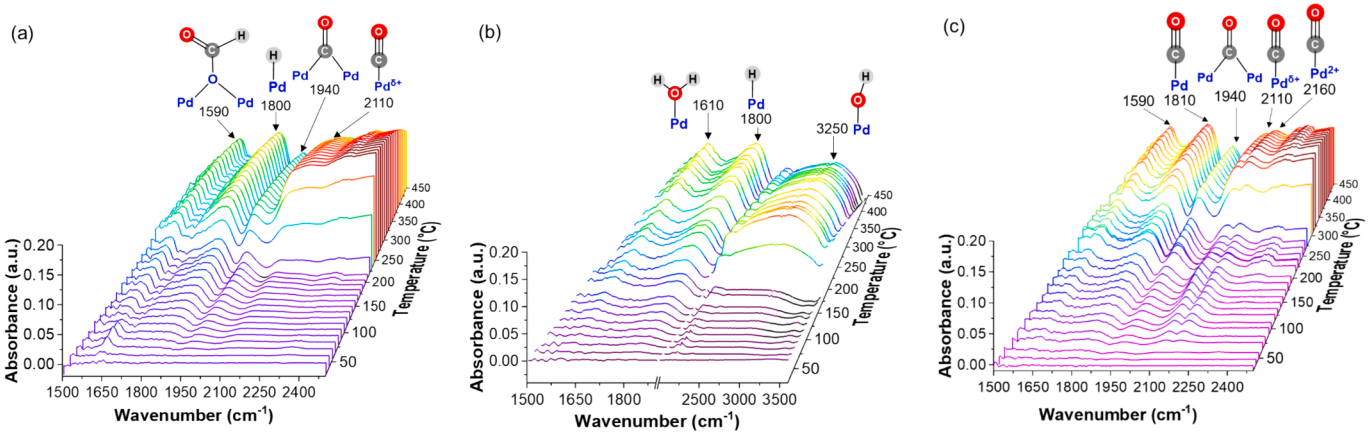

Fig. 9. In-situ DRIFTS profiles for the adsorption of (a) 37 wt% HCHO, (b) 1% H_2 with water vapor, and (c) 1% CO with water vapor. The heating rate was set at 10 °C/min.

metallic Pd^0 (JCPDS: 95–900-9521) is the only Pd-bearing species in all the spent catalysts, confirming an in-situ reduction of PdO species under the cellulose pyrolysis condition, although the oxygenates and oxidising gases such as steam is predominant. The XPS surface analysis of Pd 3d in Fig. 6**(c)** confirmed the presence of 55.2% metallic Pd^0 in the spent catalyst, along with 44.8% PdO_2. The TEM observation in Fig. 6**(d)** also confirmed the presence of Pd^0 and PdO, with rings corresponding to the Pd (1 0 0), (0 1 2), (1 1 2), and PdO (1 1 2) and (0 2 0). Statistic counting inset in Fig. 6**(e)** confirmed a relatively broad size distribution for Pd in the spent catalyst, with a relatively bimodal distribution for two peaks of ~4.5 nm and 7 nm, respectively. Likewise, based on the XRD pattern, the Pd crystallite size was confirmed to gradually increase from 8.1 nm in fresh catalyst to 10.3 nm, 11.3 nm, and 12.7 nm after each cycle (detailed in **Table S7**). Presumably, upon in-situ reduction, the resultant Pd^0 lost its surrounding oxygen atom, and subsequently aggregated.

To confirm that the reduction of PdO is one of the principal causes for catalyst deactivation, the fresh Pd-MCM-41 was purposely reduced by 5% H_2 at 400 °C, resulting in a new catalyst rPd-MCM-41. As in Fig. 7**(a)**, metallic Pd^0 (96–901-2963) was confirmed to be the sole Pd-bearing species in fresh rPd-MCM-41 and all its spent counterparts after the cyclic tests. For the activity test results in Fig. 7**(b)**, the first use of fresh rPd-MCM-41 resulted in a 54.6% selectivity and 29.8 wt% yield for furfural. Both values are considerably lower than that of the fresh Pd-MCM-41 catalyst for a selectivity of ~60% and yield of ~33 wt% for furfural (Fig. 6**(a)**). Instead, its activity is very much in line with the spent Pd-MCM-41 in Fig. 6**(a)**, where the selectivity of 54.1% and yield of 28.8 wt% were witnessed in the second cycle. These results provide strong evidence for PdO as the active site during cellulose pyrolysis. More interestingly, upon a subsequent regeneration at 500 °C for 30 min in air, the catalyst activity was restored back to the same level as the fresh one, as evident in Fig. 7**(c)**. The regenerated catalyst, through three consecutive reaction – regeneration cycles, demonstrated nearly consistent selectivity and yield of furfural as its fresh counterpart. Through characterisation of the regenerated catalysts including XRD in Fig. 7**(d)**, TEM in Fig. 7**(e)**, BET in **Fig. S18**, XPS Pd $3d_{3/2}$ in **Fig. S19**, CHNS in **Table S7**, and CO-pulse, we also confirmed that nearly all the physical properties of the catalyst are restored back to the original state, including an averaged particle size of ~5.3 nm for Pd, surface dispersion of ~44.4% and an average pore size of 3.7 nm that are all nearly identical with the fresh one (Table 1). The XPS surface analysis of Pd 3d confirmed the primary existence of 78.7% Pd^{4+} as PdO_2 in the regenerated catalyst, along with the presence of 21.3% PdO_x ($0 < x < 1$). Compared to the fresh Pd-MCM-41 catalyst, the slight drop on the BET surface area and total pore volume could be due to the regeneration condition which is not optimised yet (hence, the MCM-41 matrix slightly collapsed). Nevertheless, it is evident that the catalyst is thermally robust and its Pd carries a strong memory back to its initial state upon the air-combustion regeneration. Inferably, this memory function should be initiated from the preferred loss of the bridging oxygen atom between Pd and Si on their interface. This is supported by the XPS Si 2p analysis of the fresh and spent Pd-MCM-41 catalysts in Fig. 7**(f)**, where the Si binding energy of the spent Pd-MCM-41 shifted to a lower position for C-Si (C-Si-O_3) in which one O atom in the tetrahedral coordination of SiO_2 was replaced by C atom [45,46]. Indeed, the XPS C 1 s for the spent Pd-MCM-41 in **Fig. S20(a)**) confirmed the formation of C-Si bonding [46]. Plus, the FTIR analysis for the spent Pd-MCM-41 in **Fig. S20(b)** confirmed that the formation of a tiny Si-CH_2 adsorption band (990 cm^{-1}) on the surface. All these results support an important role of the Pd-O-Si interface on the fresh Pd-MCM-41 catalyst, which is clearly the primary sites for the adsorption and surface reactions during the cellulose pyrolysis.

3.4.2. *In-situ reduction of PdO in Pd-MCM-41*

Given that PdO serves as the active site, it is imperative to investigate the rationale behind the reduction of PdO during cellulose pyrolysis. In this regard, in-situ synchrotron XRD was conducted during the temperature-programmed heating of fresh Pd-MCM-41 catalyst, with and without the presence of cellulose. As in Fig. 8**(a)** for the blending of cellulose with fresh catalyst, at the starting temperature of 100 °C, the featuring patterns of PdO are present at 16.92°, 20.85°, 26.85°, 29.65°, and 34.23°, which are accompanied by SiO_2 at 10.76°, and cellulose at 7.90°, 10.19°, 11.45°, 17.18°, and 22.40° (same peaks were confirmed for pure cellulose in **Fig. S21**). Remarkably, with the temperature increasing to 250 °C, the cellulose characteristic peaks diminished, suggesting the start of cellulose pyrolysis. Simultaneously, the intensity of the PdO characteristic peaks decreased, which is accompanied by metallic Pd^0 at 19.53°, 22.59°, 32.16°, and 37.91°. These peaks also remained stable until 450 °C. In contrast, in the absence of cellulose in Fig. 8**(b)**, the temperature-programmed heating of Pd-MCM-41 in N_2 failed to show any phase change for PdO. Clearly, the reducing species such as HCHO, H_2, and CO generated from cellulose pyrolysis are more accountable for the reduction of PdO. These species are also preferentially adsorbed on the PdO active sites on the Pd-O-Si interface. Regarding the HCHO fragment derived from the Grob fragmentation reaction, its decomposition per **Eq. (9)** below, could lead to the subsequent reduction of PdO by the resultant H_2 and CO via **Eqs. (10) and (11)**. In addition, the oxidation of HCHO by the lattice oxygen of PdO could also occur, leading to the products of CO_2 and H_2O per **Eq. (12)** below. This phenomenon even occurs on the supported noble metal catalysts at room temperature [47,48].

$$HCHO_{(ad)} \rightarrow CO_{(ad)} + 2H_{(ad)} \quad (9)$$

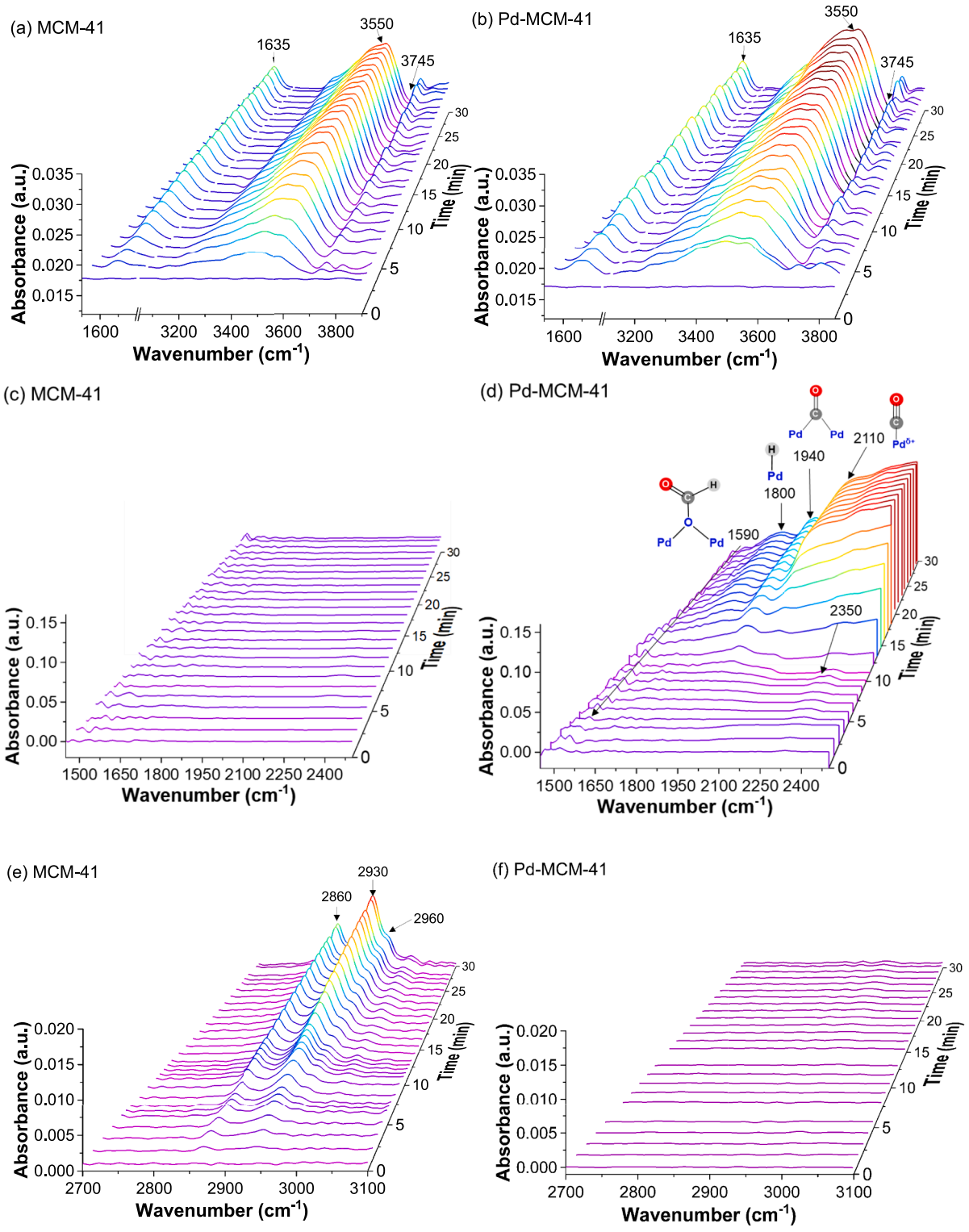

Fig. 10. In-situ DRIFTS spectra of water adsorption on (a) MCM-41 and (b) Pd-MCM-41; HCHO adsorption on (c) MCM-41 and (d) Pd-MCM-41; and furfural adsorption on (e) MCM-41 and (f) Pd-MCM-41.

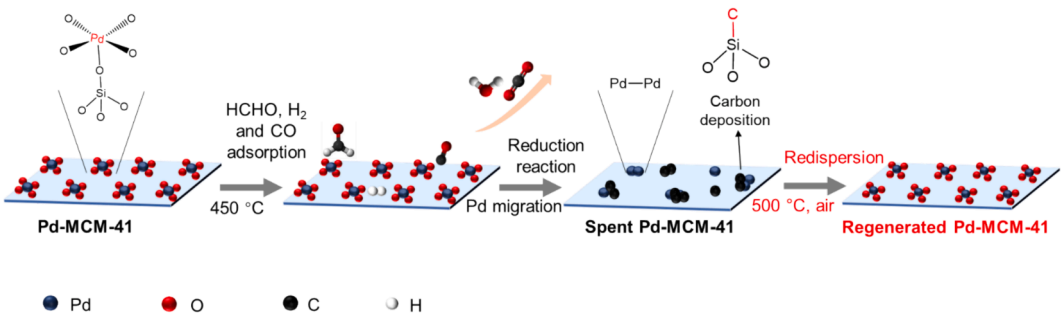

Fig. 11. Proposed scheme for the alternation between PdO and Pd^0 and its redispersion during the reaction-regeneration cycle on the Pd-MCM-41 catalyst surface.

$$2H_{(ad)} + O_{(l)} \rightarrow H_2O_{(ad)} \quad (10)$$

$$CO_{(ad)} + O_{(l)} \rightarrow CO_{2(ad)} \quad (11)$$

$$HCHO_{(ad)} + 2O_{(l)} \rightarrow CO_{2(ad)} + H_2O_{(ad)} \quad (12)$$

Where the symbol *ad* stands for the adsorbed state, and *l* for lattice oxygen of PdO which also includes the bridging oxygen between Si and Pd illustrated in Fig. 2**(d)**.

To confirm these two speculated reactions, temperature-programmed adsorption of the three reducing species were individually performed via in-situ DRIFTS. Regarding the adsorption of HCHO vapor in Fig. 9**(a)**, the adsorption at 1590 cm^{-1} for asymmetric COO stretching indicates the presence of formate for the adsorbed HCHO [49,50], whilst the adsorption bands at 1800 cm^{-1}, 1940 cm^{-1}, and 2110 cm^{-1} refer to the formation of hydride (H-Pd) for the uptake of hydrogen on metallic Pd^0, CO bonding on metallic Pd^0, and linearly bound CO on $Pd^{\delta+}$, respectively [50–52]. More notably, a baseline shift was detected from 225 ℃ onwards, which is an indicator of the reduction of PdO to Pd^0 leading to the variation in the refractive index of the material [53,54]. This transition temperature also nicely agrees with the high-temperature XRD observation in Fig. 8**(a)**. Regarding the two reducing gases, H_2 and CO, each gas (1%) was bubbled with water vapor with an approximate 3 vol% concentration before entering the in-situ DRIFTS chamber. This is to mimic the abundance of water vapor derived from the dehydration of cellulose. Clearly, as in Fig. 9**(b) and (c)**, the uplift of the baseline for the reduction of PdO into metallic Pd^0 was further confirmed. The use of H_2 induced a transition temperature of around 200 ℃, in comparison to the temperature of 300 ℃ observed upon the use of CO. The adsorption bands induced by the two reducing gases are also mostly in line with the adsorption of HCHO in Fig. 9**(a)**. Regarding the extra adsorption bands such as 1610 cm^{-1} and 3250 cm^{-1} in Fig. 9**(b)**, they refer to the stretching of OH and H_2O molecules formed by the oxidation of PdO by H_2 [53,54]. Likewise, for the extra bands including 1940 cm^{-1} and 2160 cm^{-1} in Fig. 9**(c)**, they can be attributed to the linear-bonded CO on Pd and PdO, respectively [51,52]. Nevertheless, their intensities are much weaker than the other two bands including 1590 cm^{-1} and 1810 cm^{-1} for the coverage of CO_2 molecules and the linear-bonded CO on the reduced Pd^0, respectively.

3.4.3. Surface adsorption of water, HCHO and furfural

Finally, it is noteworthy that, the variation in product distribution observed in cellulose pyrolysis over MCM-41 and Pd-MCM-41 may not only be ascribed to the Pd-centred active site, but also to the difference of the hydrophilicity of their surfaces. For the overall conversion of cellulose to furfural, the cellulose feedstock, its glucose monomers, and the intermediate LGA are highly water soluble. Therefore, a hydrophilic surface is beneficial for their initial adsorption and subsequent reactions.

In-situ DRIFTS isothermal measurements were conducted to examine the surface properties of MCM-41 and Pd-MCM-41 for the adsorption of water and HCHO at 200 °C. Regarding the continuous flow of water vapor through the catalyst surface, as in Fig. 10**(a) and (b)**, a broad range of adsorption bands for water vapor can be assigned at ~1635 cm^{-1}, ~3550 cm^{-1}, and ~3745 cm^{-1} [55,56]. **Fig. S22** quantitively confirmed a noticeable stronger intensity for the middle band over Pd-MCM-41 than that of MCM-41, supporting an enhanced hydrophilicity of the MCM-41 surface upon the doping of Pd species even in a tiny amount. Additionally, the temperature-programmed desorption of water vapor was investigated by in-situ DRIFTS. As shown in **Fig. S23(a) and (b)**, the desorption of water vapor from Pd-MCM-41 occurs at a higher temperature than from MCM-41, further supporting a stronger adsorption of water vapor on the former catalyst surface.

For the adsorption of HCHO, as in Fig. 10**(c)**, there is no discernible peak associated with HCHO in the whole duration of 30 min on the surface of MCM-41. In contrast, for the Pd-MCM-41 catalyst in Fig. 10 **(d)**, a variety of peaks appeared in 15 min, which are also in line with those confirmed for the temperature-programmed adsorption of HCHO in Fig. 9**(a)**. Presumably, this species is preferentially adsorbed on PdO site. The adsorption propensity of the target product furfural at 200 °C is also intriguing. As in Fig. 10**(e) and (f)**, the adsorption of furfural is distinct on the surface of MCM-41, showing three feature bands including 2860 cm^{-1} and 2930 cm^{-1} for the −C=C− stretch, and 2960 cm^{-1} for its aldehyde group (–CH=O) [57,58]. These adsorption bands also grew stably with the elongation of the exposure time. In contrast, for the Pd-MCM-41 surface, the adsorption band of furfural is even invisible in the whole 30 min. Moreover, the adsorption of furfural at 20 °C was investigated and the results are shown in **Fig. S23(c) and (d)**. Interestingly, no peaks were found on both catalysts, which may suggest a very weak Van der Waals force for the adsorption of furfural at low temperature. Regarding the strong adsorption bands for furfural on the MCM-41 surface at 200 °C (Fig. 10**(e)**), it should be caused by the chemical adsorption. This strong adsorption should lead to the decomposition of furfural and even deactivation of MCM-41 for the larger coke deposition on it.

3.4.4. Schematic on the phase change of Pd-MCM-41 catalyst

Based on the detailed characterisation results, Fig. 11 summarises the phase change of the Pd-MCM-41 catalyst during the fast pyrolysis of cellulose, and its reactivation upon a subsequent combustive regeneration. It is conclusive that the loading of 1 mol% Pd, although tiny, is beneficial in enhancing the hydrophilicity of the MCM-41 surface, thereby promoting the adsorption of feedstock and HCHO molecules in the vicinity of Pd-centred sites, whilst repelling the target product furfural readily. However, this triggered an in-situ reduction of PdO and the loss of the bridging oxygen atom to silica matrix via the reduction by the HCHO fragment, H_2 and/or CO. In addition, coking of the heavy compounds is induced in the vicinity of the active site. Consequently, the resultant metallic Pd^0 is less active, and aggregates. Nevertheless, the catalyst was proven to have a memory function, with its dominance of PdO and high dispersion being restored easily upon a mild combustion regeneration approach. Accordingly, the catalyst reactivity can be

restored as well.

4. Conclusions

A facile loading of MCM-41 silica support with 1 mol% Pd was attempted to maximise the production of furfural from cellulose via fast pyrolysis. Advanced reactor systems and full-picture product distribution analysis were employed to elaborate the reaction pathways. Detailed characterisation of both fresh, spent, and regenerated catalysts was conducted to reveal the active site and the phase change of Pd. The major conclusions can be drawn as follows:

1) The as-prepared facile Pd-MCM-41 catalyst achieved a high selectivity of 47.5–58.5% and a yield of 31.3–32.5 wt% for furfural. It is distinct in catalysing a direct conversion of cellulose to furfural over the C6 by-products including LGO, 5-HMF, and 5-MF. The catalyst is also relatively stable, with a slower deactivation rate than the MCM-41 reference.
2) Cationic Pd^{2+} as PdO was found to be the active site, which was readily deactivated by the coke deposition. In addition, it was reduced to metallic Pd^0 by the adsorbed HCHO molecule and even the gaseous products including H_2 and CO on the Pd-O-Si interface. Nevertheless, mild combustion regeneration is effective in restoring the catalyst activity, due to a strong memory of the catalyst which is in favour of restoring the active phase, Pd dispersion, and size during the regeneration process.
3) The loading of 1 mol% Pd is effective in enhancing the surface hydrophilicity of MCM-41 support, promoting the adsorption and subsequent decompositions of the undesired formaldehyde (HCHO), as well as the desorption of furfural product which otherwise would undertake excessive secondary reactions on the original hydrophobic MCM-41 surface.

CRediT authorship contribution statement

Jingwei Wang: Writing – original draft, Methodology, Formal analysis, Data curation. **Qiaoqiao Zhou:** Writing – review & editing, Supervision, Methodology, Formal analysis, Conceptualization. **Jinxing Gu:** Writing – review & editing, Methodology. **Sasha Yang:** Writing – review & editing, Supervision, Methodology, Formal analysis. **Qinfen Gu:** Writing – review & editing, Software, Resources, Methodology. **Anthony De Girolamo:** Writing – review & editing, Resources. **Lian Zhang:** Writing – review & editing, Supervision, Resources, Funding acquisition, Conceptualization.

Declaration of competing interest

The authors declare that they have no known competing financial interests or personal relationships that could have appeared to influence the work reported in this paper.

Data availability

Data will be made available on request.

Acknowledgments

This work was funded by the Australian Research Council (ARC) Linkage Project (LP220100365). The HT-XRD and XAS analysis were undertaken on the Powder Diffraction beamline and X-ray Absorption Spectroscopy beamline under the Australian Synchrotron beamtime awards of M19819 and M18547, respectively. The first author would like to acknowledge the Australian Carbon Innovation (ACI) top-up Scholarship for her Ph.D. living allowance support. The authors would also like to acknowledge Dr Tim Williams and Dr Nick McDougall in Monash Centre of Electron Microscopy (MCEM), Monash University for their assistance with TEM and SEM analysis, respectively. Ms Yvonne Hora in Monash X-ray Platform (MXP) is also acknowledged for her help on the XPS spectra collection.

Appendix A. Supplementary data

Supplementary data to this article can be found online at https://doi.org/10.1016/j.cej.2024.154314.

References

[1] L. Dai, Y. Wang, Y. Liu, C. He, R. Ruan, Z. Yu, L. Jiang, Z. Zeng, Q. Wu, A review on selective production of value-added chemicals via catalytic pyrolysis of lignocellulosic biomass, Sci. Total Environ. 749 (2020) 142386, https://doi.org/10.1016/j.scitotenv.2020.142386.
[2] C. del Pozo, F. Rego, Y. Yang, N. Puy, J. Bartrolí, E. Fàbregas, A.V. Bridgwater, Converting coffee silverskin to value-added products by a slow pyrolysis-based biorefinery process, Fuel Process. Technol. 214 (2021) 106708, https://doi.org/10.1016/j.fuproc.2020.106708.
[3] J. Zhu, G. Yin, Catalytic Transformation of the Furfural Platform into Bifunctionalized Monomers for Polymer Synthesis, ACS Catal. 11 (15) (2021) 10058–10083, https://doi.org/10.1021/acscatal.1c01989.
[4] K. Yan, G. Wu, T. Lafleur, C. Jarvis, Production, properties and catalytic hydrogenation of furfural to fuel additives and value-added chemicals, Renew. Sustain. Energy Rev. 38 (2014) 663–676, https://doi.org/10.1016/j.rser.2014.07.003.
[5] J. Fermoso, P. Pizarro, J.M. Coronado, D.P. Serrano, Advanced biofuels production by upgrading of pyrolysis bio-oil, WIREs Energy Environ. 6 (4) (2017) e245.
[6] Furfural Market: Global Industry Trends, Share, Size, Growth, Opportunity and Forecast 2023-2028. (Accessed 2023).
[7] Q. Zhou, Z. Liu, T.Y. Wu, L. Zhang, Furfural from pyrolysis of agroforestry waste: Critical factors for utilisation of C5 and C6 sugars, Renew. Sustain. Energy Rev. 176 (2023) 113194, https://doi.org/10.1016/j.rser.2023.113194.
[8] C. Li, J. Zhang, J. Gu, H. Yuan, Y. Chen, Insight into the role of varied acid-base sites on fast pyrolysis kinetics and mechanism of cellulose, Waste Manag. 135 (2021) 140–149, https://doi.org/10.1016/j.wasman.2021.08.040.
[9] C. Li, C. Zhang, G. Gao, M. Gholizadeh, S. Zhang, L. Xu, L. Zhang, Q. Li, X. Hu, Interaction of the volatiles from co-pyrolysis of pig manure with cellulose/glucose and their effects on char properties, J. Environ. Chem. Eng. 8 (6) (2020) 104583, https://doi.org/10.1016/j.jece.2020.104583.
[10] B. Hu, Q. Lu, Y.-T. Wu, W.-L. Xie, M.-S. Cui, J. Liu, C.-Q. Dong, Y.-P. Yang, Insight into the formation mechanism of levoglucosenone in phosphoric acid-catalyzed fast pyrolysis of cellulose, J. Energy Chem. 43 (2020) 78–89, https://doi.org/10.1016/j.jechem.2019.08.001.
[11] Q. Zhou, J. Gu, J. Wang, A. De Girolamo, S. Yang, L. Zhang, High production of furfural by flash pyrolysis of C6 sugars and lignocellulose by Pd-PdO/$ZnSO_4$ catalyst, Nat. Commun. 14 (1) (2023) 1563, https://doi.org/10.1038/s41467-023-37250-0.
[12] X. Bai, J. Li, C. Jia, J. Shao, Q. Yang, Y. Chen, H. Yang, X. Wang, H. Chen, Preparation of furfural by catalytic pyrolysis of cellulose based on nano Na/Fe-solid acid, Fuel 258 (2019) 116089, https://doi.org/10.1016/j.fuel.2019.116089.
[13] D. Minoli, Nanotechnology Applications to Telecommunications and Networking, Wiley, Daniel Minoli, 2005.
[14] S.J. You, E.D. Park, Effects of dealumination and desilication of H-ZSM-5 on xylose dehydration, Microporous Mesoporous Mater. 186 (2014) 121–129, https://doi.org/10.1016/j.micromeso.2013.11.042.
[15] S. Kaiprommarat, S. Kongparakul, P. Reubroycharoen, G. Guan, C. Samart, Highly efficient sulfonic MCM-41 catalyst for furfural production: Furan-based biofuel agent, Fuel 174 (2016) 189–196, https://doi.org/10.1016/j.fuel.2016.02.011.
[16] C.A. Koh, R. Nooney, S. Tahir, Characterisation and catalytic properties of MCM-41 and Pd/MCM-41 materials, Catal. Lett. 47 (3) (1997) 199–203, https://doi.org/10.1023/A:1019025609426.
[17] J. Panpranot, K. Pattamakomsan, J.G. Goodwin, P. Praserthdam, A comparative study of Pd/SiO_2 and Pd/MCM-41 catalysts in liquid-phase hydrogenation, Catal. Commun. 5 (10) (2004) 583–590, https://doi.org/10.1016/j.catcom.2004.07.008.
[18] W. Zou, Y. Liu, C. Song, H. Lin, H. Huang, W. Ye, R. Lu, S. Zhang, In situ reduction of PdO encapsulated in MCM-41 to Pd^0 for dehydrogenation of formic acid, Int. J. Hydrogen Energy 47 (66) (2022) 28518–28529, https://doi.org/10.1016/j.ijhydene.2022.06.190.
[19] A. Na Rungsi, T.H. Truong, C. Thunyaratchatanon, A. Luengnaruemitchai, N. Chollacoop, S.-Y. Chen, T. Mochizuki, H. Takagi, Y. Yoshimura, Tuning the porosity of sulfur-resistant Pd-Pt/MCM-41 bimetallic catalysts for partial hydrogenation of soybean oil-derived biodiesel, Fuel 298 (2021) 120658, https://doi.org/10.1016/j.fuel.2021.120658.
[20] X. Liu, C. Wang, Y. Chen, Q. Qin, Y. Li, H. He, Formaldehyde oxidation on Pd/USY catalysts at room temperature: The effect of acid pretreatment on supports, J. Environ. Sci. 125 (2023) 811–822, https://doi.org/10.1016/j.jes.2022.02.025.
[21] G. Li, L. Li, Highly efficient formaldehyde elimination over meso-structured M/CeO2 (M = Pd, Pt, Au and Ag) catalyst under ambient conditions, RSC Adv. 5 (46) (2015) 36428–36433, https://doi.org/10.1039/C5RA04928H.
[22] H. Alamgholiloo, N.N. Pesyan, S. Rostamnia, A novel strategy for stabilization of sub-nanometric Pd colloids on kryptofix functionalized MCM-41: nanoengineered

material for Stille coupling transformation, Sci. Rep. 11 (1) (2021) 18417, https://doi.org/10.1038/s41598-021-97914-z.
[23] J. Garcia-Aguilar, M. Navlani-Garcia, A. Berenguer-Murcia, K. Mori, Y. Kuwahara, H. Yamashita, D. Cazorla-Amoros, Evolution of the PVP-Pd surface interaction in nanoparticles through the case study of formic acid decomposition, Langmuir 32 (46) (2016) 12110–12118, https://doi.org/10.1021/acs.langmuir.6b03149.
[24] J.V. Jayarama Krishna, O.P. Korobeinichev, R. Vinu, Isothermal fast pyrolysis kinetics of synthetic polymers using analytical Pyroprobe, J. Analyt. Appl. Pyrol. 139 (2019) 48–58, https://doi.org/10.1016/j.jaap.2019.01.008.
[25] V.S. Sikarwar, M. Zhao, P. Clough, J. Yao, X. Zhong, M.Z. Memon, N. Shah, E. J. Anthony, P.S. Fennell, An overview of advances in biomass gasification, Energ. Environ. Sci. 9 (10) (2016) 2939–2977, https://doi.org/10.1039/C6EE00935B.
[26] E. Dündar-Tekkaya, Y. Yürüm, Mesoporous MCM-41 material for hydrogen storage: A short review, Int. J. Hydrogen Energy 41 (23) (2016) 9789–9795, https://doi.org/10.1016/j.ijhydene.2016.03.050.
[27] K.M. Khalil, Cerium modified MCM-41 nanocomposite materials via a nonhydrothermal direct method at room temperature, J. Colloid Interface Sci. 315 (2) (2007) 562–568, https://doi.org/10.1016/j.jcis.2007.07.030.
[28] A. Ghosh, C. Ranjan Patra, P. Mukherjee, M. Sastry, R. Kumar, Preparation and stabilization of gold nanoparticles formed by in situ reduction of aqueous chloroaurate ions within surface-modified mesoporous silica, Micropor. Mesopor. Mater. 58(3) (2003) 201-211. https://doi.org/10.1016/s1387-1811(02)00626-1.
[29] Z. Ping Xu, C. Yew Mok, W. Shong Chin, H. Hua Huang, S. Li, W. Huang, Interconversion and decomposition of furanones, J. Chem. Soc., Perkin Transact. 2 (4) (1999) 725–730, https://doi.org/10.1039/A810028D.
[30] X. Wei, Z. Wang, Y. Wu, Z. Yu, J. Jin, K. Wu, Fast pyrolysis of cellulose with solid acid catalysts for levoglucosenone, J. Anal. Appl. Pyrol. 107 (2014) 150–154, https://doi.org/10.1016/j.jaap.2014.02.015.
[31] A.I. Casoni, M.L. Nievas, E.L. Moyano, M. Álvarez, A. Diez, M. Dennehy, M. A. Volpe, Catalytic pyrolysis of cellulose using MCM-41 type catalysts, Appl. Catal. A 514 (2016) 235–240, https://doi.org/10.1016/j.apcata.2016.01.017.
[32] W. Prationo, J. Zhang, J. Cui, Y. Wang, L. Zhang, Influence of inherent moisture on the ignition and combustion of wet Victorian brown coal in air-firing and oxy-fuel modes: Part 1: the volatile ignition and flame propagation, Fuel Process. Technol. 138 (2015) 670–679, https://doi.org/10.1016/j.fuproc.2015.07.008.
[33] D.K. Shen, S. Gu, The mechanism for thermal decomposition of cellulose and its main products, Bioresour. Technol. 100 (24) (2009) 6496–6504, https://doi.org/10.1016/j.biortech.2009.06.095.
[34] L. Zhang, H. Yu, P. Wang, Y. Li, Production of furfural from xylose, xylan and corncob in gamma-valerolactone using $FeCl_3{\cdot}6H_2O$ as catalyst, Bioresour. Technol. 151 (2014) 355–360, https://doi.org/10.1016/j.biortech.2013.10.099.
[35] J. Cui, J. Tan, T. Deng, X. Cui, Y. Zhu, Y. Li, Conversion of carbohydrates to furfural via selective cleavage of the carbon–carbon bond: the cooperative effects of zeolite and solvent, Green Chem. 18 (6) (2016) 1619–1624, https://doi.org/10.1039/C5GC01948F.
[36] K. Djakaria, Z. Tang, J. Shao, X. Chen, H. Xiao, J. Smith, H. Yang, H. Chen, Improving the production of furfural from cellulose catalytic pyrolysis using WO3/γ-Al2O3 composite oxides, J. Anal. Appl. Pyrol. 167 (2022) 105648, https://doi.org/10.1016/j.jaap.2022.105648.
[37] Z. Song, C. Yang, B. Yang, H. Luo, B. Zhang, Y. Zhang, R. Li, Q. Qiu, Y. Ding, Effects of Cd and Sn modified MCM-41 on pyrolysis of cellulose, J. Renew. Sustain. Energy 13 (1) (2021) 013101, https://doi.org/10.1063/5.0030180.
[38] F. Cao, S. Xia, X. Yang, C. Wang, Q. Wang, C. Cui, A. Zheng, Lowering the pyrolysis temperature of lignocellulosic biomass by H2SO4 loading for enhancing the production of platform chemicals, Chem. Eng. J. 385 (2020) 123809, https://doi.org/10.1016/j.cej.2019.123809.
[39] Y. Chi, J. Xue, J. Zhuo, D. Zhang, M. Liu, Q. Yao, Catalytic co-pyrolysis of cellulose and polypropylene over all-silica mesoporous catalyst MCM-41 and Al-MCM-41, Sci. Total Environ. 633 (2018) 1105–1113, https://doi.org/10.1016/j.scitotenv.2018.03.239.
[40] X. Chen, Y. Chen, Z. Chen, D. Zhu, H. Yang, P. Liu, T. Li, H. Chen, Catalytic fast pyrolysis of cellulose to produce furan compounds with SAPO type catalysts, J. Analyt. Appl. Pyrolys. 129 (2018) 53–60, https://doi.org/10.1016/j.jaap.2017.12.004.
[41] X. Chen, H. Yang, Y. Chen, W. Chen, T. Lei, W. Zhang, H. Chen, Catalytic fast pyrolysis of biomass to produce furfural using heterogeneous catalysts, J. Anal. Appl. Pyrol. 127 (2017) 292–298, https://doi.org/10.1016/j.jaap.2017.07.022.
[42] E.M. Prosen, D. Radlein, J. Piskorz, D.S. Scott, R.L. Legge, Microbial utilization of levoglucosan in wood pyrolysate as a carbon and energy source, Biotechnol. Bioeng. 42 (4) (1993) 538–541, https://doi.org/10.1002/bit.260420419.
[43] X. Huang, J. Ren, J.-Y. Ran, C.-L. Qin, Z.-Q. Yang, J.-P. Cao, Recent advances in pyrolysis of cellulose to value-added chemicals, Fuel Process. Technol. 229 (2022) 107175, https://doi.org/10.1016/j.fuproc.2022.107175.
[44] J. Wurmel, J.M. Simmie, M.M. Losty, C.D. McKenna, Thermal decomposition of 2 (3H) and 2(5H) furanones: theoretical aspects, Chem. A Eur. J. 119 (26) (2015) 6919–6927, https://doi.org/10.1021/acs.jpca.5b04435.
[45] G.G. Lara, G.F. Andrade, M.F. Cipreste, W.M. da Silva, P.L. Gastelois, D.A. Gomes, M.C. de Miranda, W.A. de Almeida Macedo, M.J. Neves, E.M.B. de Sousa, Protection of normal cells from irradiation bystander effects by silica-flufenamic acid nanoparticles, J. Mater. Sci. - Mater. Med. 29 (8) (2018) 130, https://doi.org/10.1007/s10856-018-6134-5.
[46] NIST X-ray Photoelectron Spectroscopy Database, NIST Standard Reference Database Number 20, National Institute of Standards and Technology, Gaithersburg MD, 2000. Doi: 10.18434/T4T88K.
[47] G.A. Attard, H.D. Ebert, R. Parsons, Formaldehyde decomposition and oxidation on Pt(110), Surf. Sci. 240 (1) (1990) 125–135, https://doi.org/10.1016/0039-6028(90)90736-R.
[48] S.J. Park, I. Bae, I.-S. Nam, B.K. Cho, S.M. Jung, J.-H. Lee, Oxidation of formaldehyde over Pd/Beta catalyst, Chem. Eng. J. 195–196 (2012) 392–402, https://doi.org/10.1016/j.cej.2012.04.028.
[49] S. Colussi, M. Boaro, L. de Rogatis, A. Pappacena, C. de Leitenburg, J. Llorca, A. Trovarelli, Room temperature oxidation of formaldehyde on Pt-based catalysts: A comparison between ceria and other supports (TiO_2, Al_2O_3 and ZrO_2), Catal. Today 253 (2015) 163–171, https://doi.org/10.1016/j.cattod.2015.02.028.
[50] G. Busca, J. Lamotte, J.C. Lavalley, V. Lorenzelli, FT-IR study of the adsorption and transformation of formaldehyde on oxide surfaces, J. Am. Chem. Soc. 109 (17) (1987) 5197–5202, https://doi.org/10.1021/ja00251a025.
[51] L.L. Sheu, H. Knozinger, W.M.H. Sachtler, Characterization by CO/FTIR spectroscopy of palladium supported on NaY zeolites, J. Mol. Catal. 57 (1) (1989) 61–79, https://doi.org/10.1016/0304-5102(89)80127-0.
[52] Y. Cao, M. Yu, S. Qi, T. Wang, S. Huang, S. Hu, M. Xu, S. Yan, Formation and evolution of orientation-specific CO_2 chains on nonpolar ZnO(1010) surfaces, Sci. Rep. 7 (2017) 43442, https://doi.org/10.1038/srep43442.
[53] T. Fovanna, I. Alxneit, A.H. Clark, S. Checchia, M. Di Michiel, O. Kröcher, M. Nachtegaal, D. Ferri, Reduction of PdO/Al_2O_3 in Liquid Cyclohexane Followed In Situ by ATR-IR, High-Energy XRD, and XAS, J. Phys. Chem. C 125 (30) (2021) 16473–16482, https://doi.org/10.1021/acs.jpcc.1c01882.
[54] C. Mondelli, D. Ferri, J. Grunwaldt, F. Krumeich, S. Mangold, R. Psaro, A. Baiker, Combined liquid-phase ATR-IR and XAS study of the Bi-promotion in the aerobic oxidation of benzyl alcohol over Pd/Al_2O_3, J. Catal. 252 (1) (2007) 77–87, https://doi.org/10.1016/j.jcat.2007.09.013.
[55] X. Song, J.F. Boily, Water vapor adsorption on goethite, Environ. Sci. Tech. 47 (13) (2013) 7171–7177, https://doi.org/10.1021/es400147a.
[56] H.A. Al-Abadleh, V.H. Grassian, FT-IR study of water adsorption on aluminum oxide surfaces, Langmuir 19 (2) (2003) 341–347, https://doi.org/10.1021/la026208a.
[57] N. Mohamad, N. Abd-Talib, T.-L. Kelly Yong, Furfural production from oil palm frond (OPF) under subcritical ethanol conditions, Materials Today: Proceedings 31 (2020) 116-121. Doi: 10.1016/j.matpr.2020.01.256.
[58] N.E. Ali Othman, Production of furfural from oil palm fibres, J. Oil Palm Res. 33(3) (2020) 473-481. Doi: 10.21894/jopr.2020.0109.